Chemical Engineering Research and Design 219 (2025) 52–66

Contents lists available at ScienceDirect

Chemical Engineering Research and Design

journal homepage: www.elsevier.com/locate/cherd

A critical analysis of multifluid turbulent models for simulating liquid–particle turbulent flows in agitated vessels

Ziming Wang, Luca Mazzei *

Department of Chemical Engineering, University College London, Torrington Place, London WC1E 7JE, UK

ARTICLE INFO

Keywords:
Agitated vessels
CFD
Liquid–particle suspensions
Multiphase turbulent flows
Multiphase turbulence modeling

ABSTRACT

This paper analyzes critically some multifluid turbulent models for liquid–particle mixtures derived from Eulerian–Eulerian laminar models. As benchmark, we use the model of Fox (2014), derived by rigorously Reynolds-averaging the Eulerian–Eulerian transport equations. The results of this model are compared to those of other models commonly used in the literature, where turbulence terms are added to the multifluid transport equations without theoretical justification. In spite of this, such models often yield good results. When in these models the mean variables are replaced with the Reynolds-averaged variables of the model by Fox (2014), the latter is not recovered, because it features various additional terms. Moreover, for some of the undetermined terms present in both models, the closures differ. Our simulations for turbulent multifluid flows in agitated vessels indicate that closures for the turbulent drift velocity impact the results negligibly, whereas those for turbulent interaction terms and drag coefficients do affect the results. With appropriate closures, the simulation results produced by the Fox (2014) model align well with experimental data, confirming the applicability of the model for the application considered. While some of the additional terms present in the Fox (2014) model have minimal impact on the results, the source term for the granular internal energy is appreciable, even if it is not sufficiently large to alter the overall simulation accuracy. These findings may explain why the other models, which do not account for various terms arising from the rigorous Reynolds-averaging procedure, do produce reasonably accurate results.

1. Introduction

Agitated vessels are extensively used to mix liquid–particle suspensions in numerous industrial applications, including crystallization, dissolution and catalytic processes. The performance of these applications depends on how well the particles are suspended and mixed in the liquid, and hence is dictated by the fluid dynamics inside the vessel. Therefore, it is crucial that this be predicted accurately.

To predict the fluid dynamics of liquid–particle mixtures, computational fluid dynamics (CFD) methods play a crucial role. Among these methods, the Eulerian–Lagrangian (also called direct numerical simulation) method is the most detailed and fundamental (Pan et al., 2002; Sardina et al., 2012; Oke et al., 2015; Feng et al., 2016; Gualtieri et al., 2017; Battista et al., 2018). This method computes velocity and pressure fields at every point occupied by the fluid by solving the usual continuity and Navier–Stokes equations, and tracks the motion (translation and rotation) of each particle by solving Newton's second law for rigid bodies. Even if it yields the most fundamental details, such as the pressure and velocity gradients over the surfaces of the particles, this approach is computationally demanding and unviable for systems with large particle numbers. Moreover, the information generated, such as the position and velocity of each particle, must be filtered to get information of interest for industrial applications, such as the solid volume fraction and mean velocity fields. To reduce the computational cost, researchers often use a hybrid modeling approach called discrete element (or unresolved Eulerian–Lagrangian) method. Here, the continuity and Navier–Stokes equations for the fluid are averaged, while the motions of the particles are still solved by employing Newton's second law for rigid bodies. Although significantly less demanding than the Eulerian–Lagrangian alternative, this method is also unviable for systems with large particle numbers and, for the solid phase, does not directly yield the desired observables (Lettieri and Mazzei, 2009; Deen et al., 2014).

To reduce the computational demand further and directly obtain the information of interest, many studies adopt the Eulerian–Eulerian method (Drew, 1983; Ahmadi and Ma, 1990; Jackson, 1997; Jamshidi et al., 2019, 2021). Here, both phases are regarded as interpenetrating continua occupying the entire physical space, their dynamics described via averaged equations of change expressed in terms of mean properties. This averaging process generates many undetermined terms, such

* Corresponding author.
E-mail address: l.mazzei@ucl.ac.uk (L. Mazzei).

https://doi.org/10.1016/j.cherd.2025.05.023
Received 15 January 2025; Received in revised form 9 May 2025; Accepted 11 May 2025
Available online 29 May 2025

as the phasic effective stress tensors and the fluid–particle interaction force (Jackson, 1997; Mazzei, 2008). To model them, different closures have been proposed, and these must be appropriately selected to ensure reliable predictions. In systems with nearly neutrally buoyant particles, if the Stokes number (the ratio of the particle relaxation time to the characteristic time scale of the flow) is much smaller than unity, the mean velocity fields of the solid and liquid phases rapidly relax to local equilibrium, and their relative velocity approaches zero. In such cases, the Eulerian–Eulerian approach can be simplified to the mixture approach, where the suspension is treated as one effective fluid. For details, see Jackson (1997, 2000) and Jamshidi et al. (2019).

In applications involving the mixing of liquid–particle suspensions in agitated vessels, both the mixture and Eulerian–Eulerian models are commonly adopted (Altway et al., 2001; Ljungqvist and Rasmuson, 2001; Oshinowo and Bakker, 2002; Kasat et al., 2008; Ochieng and Onyango, 2008; Shan et al., 2008; Jiang and Zhang, 2012; Wadnerkar et al., 2012; Calvo et al., 2013; Liu and Barigou, 2014; Tamburini et al., 2014; Wadnerkar et al., 2016; Wang et al., 2017; Delafosse et al., 2018; Maluta et al., 2019; Shi and Rzehak, 2020). At large solid volume fractions, when particle collisions significantly affect the solid effective stress tensor and in turn the fluid dynamics in the vessel, a balance equation for the granular internal energy must be included in the set of transport equations. In commercial CFD codes, this makes implementing the mixture model complex, so that the Eulerian–Eulerian model is usually more convenient. In this work, the system of interest makes the mixture model inapplicable (the particles are not nearly neutrally buoyant and the Stokes number is not much smaller than unity); consequently, we adopt the Eulerian–Eulerian model.

In agitated vessels, the impeller rotation often generates large mean velocities in both phases, leading to high Reynolds numbers (based on the impeller size as characteristic length). Thus, the average fluid dynamic variables are turbulent. In each phase, turbulence is characterized by rapid fluctuations (in time and space) of the mean (or, equivalently, Eulerian) variables, such as the volume fractions and mean velocities (Dasgupta et al., 1994, 1998; Fox, 2014). These fluctuations can be fully captured by the Eulerian–Eulerian (or, when it is applicable, by the mixture) model, provided that the time step is small enough and the computational grid is sufficiently fine. However, this renders this approach too demanding, making it impractical. To reduce the computational cost, one can average the Eulerian–Eulerian equations of change (Dasgupta et al., 1994, 1998; Fox, 2014). To do so, volume, time and Reynolds (ensemble) averaging schemes can be employed. But since the first two are rigorous solely for statistically homogeneous and stationary flows, respectively (Pope, 2000; Fox, 2003, 2014), here we opt for the more general Reynolds averaging method. The specifics of this method are detailed in Section 2.

In the literature, many studies did not employ turbulent multifluid transport equations rigorously derived by averaging the (laminar) Eulerian–Eulerian equations of change. They instead assumed that the latter could be directly applied to simulate liquid–particle turbulent flows by simply introducing specific terms to account for the effects of turbulence. As in these models the Eulerian–Eulerian equations of change are not averaged further, we refer to them as *one-step averaging models*. In these models, the kinetic stress tensor of the solid phase, related to the particle velocity fluctuations, is often incorrectly related to turbulence and interpreted as a kind of Reynolds stress contribution (see, for instance, Drew, 1983; Ahmadi and Ma, 1990; Enwald et al., 1996; Peirano and Leckner, 1998). Consequently, the granular temperature and the turbulent kinetic energy of the solid phase, along with their sources and sinks, are modeled incorrectly (Fox, 2014). In other versions of one-step averaging models, even if this conceptual error is absent, the transport equations miss various terms that the properly-derived Reynolds-averaged equations feature. Nevertheless, these models are widely used for simulating liquid–particle turbulent flows in agitated vessels and often do provide satisfactory results (see, for instance, Jiang and Zhang, 2012; Wadnerkar et al., 2012, 2016; Delafosse et al., 2018; Maluta et al., 2019). In Section 2.1.3, we discuss these models in more detail, and in the rest of the article we investigate why, in spite of their shortcomings, they can give good predictions.

To our knowledge, even if the turbulent multifluid model derived by Reynolds averaging the equations of the Eulerian–Eulerian model is theoretically rigorous, it has been rarely employed to simulate liquid–particle turbulent flows in agitated vessels. In addition, the distinction between this model and the one-step averaging ones remains unexplored. The comparison between them might explain why the latter can yield good results. This study aims to address this research gap by delving into the details of these models, contrasting them via simulations of a selected experimental study. The article is structured as follows. In Section 2, we introduce the transport and closure equations for the Eulerian–Eulerian and turbulent multifluid models; in Section 3, we detail the conditions of the selected experiments and the computational setup; in Section 4, we present a comparative analysis, contrasting the simulation results of the models, assessing them against experimental data taken from the literature, and evaluating their accuracy.

2. Multifluid models

As discussed, simulating liquid–particle turbulent flows in agitated vessels using the Eulerian–Eulerian model with a fine mesh and small computational time steps is extremely demanding computationally. To overcome this challenge, we resort to turbulent multifluid models, which should be derived by Reynolds averaging the Eulerian–Eulerian equations of change. In this section, we first briefly present these equations of change and then discuss the Reynolds averaging processes; additionally, we describe how one-step averaging models are developed. The section concludes with a discussion of the closures required to make the governing equations of these models solvable.

2.1. Governing equations

2.1.1. Eulerian-Eulerian (or multifluid) model

We consider an isothermal liquid–particle suspension composed of an incompressible Newtonian liquid and spherical particles of uniform size and density. The point (that is, non-averaged) balance equations of mass and linear momentum for the liquid read:

$$\partial_{\boldsymbol{x}} \cdot \bar{\boldsymbol{u}}_e = 0 \tag{2.1}$$

$$\rho_e \partial_t \bar{\boldsymbol{u}}_e = -\rho_e \partial_{\boldsymbol{x}} \cdot \bar{\boldsymbol{u}}_e \bar{\boldsymbol{u}}_e - \partial_{\boldsymbol{x}} \cdot \bar{\boldsymbol{\sigma}}_e + \rho_e \boldsymbol{g} \tag{2.2}$$

where ρ_e, $\bar{\boldsymbol{u}}_e$ and $\bar{\boldsymbol{\sigma}}_e$ are the density, point velocity and point stress tensor of the liquid, respectively, and $\boldsymbol{g}$ is the gravitational field. To derive the Eulerian–Eulerian equations of change, one has to average Eqs. (2.1) and (2.2). Various averaging methods can be used, but the resulting equations are quite similar and share common features (Jackson, 1997, 2000; Zhang and Prosperetti, 1997). Here, we refer to the method adopted by Jackson (1997), based on soft volume averages, which yields:

$$\partial_t \alpha_e = -\partial_{\boldsymbol{x}} \cdot \alpha_e \boldsymbol{u}_e \tag{2.3}$$

$$\rho_e \partial_t (\alpha_e \boldsymbol{u}_e) = -\rho_e \partial_{\boldsymbol{x}} \cdot \alpha_e \boldsymbol{u}_e \boldsymbol{u}_e - \partial_{\boldsymbol{x}} \cdot \boldsymbol{S}_e - \boldsymbol{f}_p + \alpha_e \rho_e \boldsymbol{g} \tag{2.4}$$

where α_e, $\boldsymbol{u}_e$ and $\boldsymbol{S}_e$ are the volume fraction, the mean (Eulerian) velocity and the effective stress tensor of the liquid phase, respectively, and $\boldsymbol{f}_p$ is the mean fluid–particle interaction force per suspension unit volume. The effective stress tensor is defined as:

$$\boldsymbol{S}_e \equiv \alpha_e \boldsymbol{\sigma}_e + \boldsymbol{S}_{e,p} + \alpha_e \rho_e \langle \hat{\boldsymbol{u}} \hat{\boldsymbol{u}} \rangle_e \tag{2.5}$$

where $\boldsymbol{\sigma}_e$ represents the mean value of $\bar{\boldsymbol{\sigma}}_e$ and $\langle \hat{\boldsymbol{u}} \hat{\boldsymbol{u}} \rangle_e$ the mean value of the dyadic product of the fluid point velocity fluctuations, $\hat{\boldsymbol{u}}_e \equiv \bar{\boldsymbol{u}}_e - \boldsymbol{u}_e$. The fluid effective stress tensor comprises three contributors. The first is related to the point stress tensor of the fluid. The second, sometimes referred to as particle-presence stress, arises from the fluid dynamic interactions between the fluid and the particles; for details,

we refer to Jamshidi et al. (2021). The third, a Reynolds stress type of contribution, results from fluid point velocity fluctuations. These fluctuations can arise from various factors, not necessarily related to turbulence, such as particle wakes and the no-slip boundary conditions holding at the particle surfaces.

For the solid phase, the volume-averaged balance equations for mass and linear momentum are derived similarly, from equations analogous to Eqs. (2.1) and (2.2) (Jamshidi et al., 2021). They read:

$$\partial_t \alpha_s = -\partial_{\boldsymbol{x}} \cdot \alpha_s \boldsymbol{u}_s \tag{2.6}$$

$$\rho_s \partial_t (\alpha_s \boldsymbol{u}_s) = -\rho_s \partial_{\boldsymbol{x}} \cdot \alpha_s \boldsymbol{u}_s \boldsymbol{u}_s - \partial_{\boldsymbol{x}} \cdot \boldsymbol{S}_s + \boldsymbol{f}_p + \alpha_s \rho_s \boldsymbol{g} \tag{2.7}$$

where α_s, $\boldsymbol{u}_s$ and $\boldsymbol{S}_s$ are the volume fraction, the mean (Eulerian) velocity and the effective stress tensor of the solid phase, respectively. $\boldsymbol{S}_s$ is defined as:

$$\boldsymbol{S}_s \equiv \boldsymbol{S}_{s,c} + \alpha_s \rho_s \langle \hat{\boldsymbol{u}} \hat{\boldsymbol{u}} \rangle_s \tag{2.8}$$

where $\langle \hat{\boldsymbol{u}} \hat{\boldsymbol{u}} \rangle_s$ represents the mean value of the dyadic product of the particle velocity fluctuations. The solid effective stress tensor comprises two contributors. The first, referred to as particle-contact stress, stems from instantaneous particle contacts (collisional stress) and enduring particle contacts (frictional stress). Of these, the latter are significant only when the solid volume fraction is close to the packing limit $\alpha_{s,max}$ (often set at 63%). In agitated vessels, this condition is typically confined to a small region near the bottom center, so the frictional stress is often neglected (Jiang and Zhang, 2012; Maluta et al., 2019; Wang et al., 2017). The second contributor to the solid effective stress tensor is referred to as kinetic stress, denoted here as $\boldsymbol{S}_{s,k}$. This arises from particle velocity fluctuations, which may stem from Brownian motion, fluctuating fluid–particle forces, average fluid dynamic shear, and particle collisions (Buyevich, 1999; Jamshidi et al., 2019). As in the kinetic theory of molecular (Chapman and Cowling, 1991) and granular (Brilliantov and Pöschel, 2004) gases, $\boldsymbol{S}_{s,k}$ is unrelated to turbulence and should not be regarded as a Reynolds stress.

The set of balance equations for mass and linear momentum is complemented by a balance equation for the granular internal energy, $(3/2)\theta_s$, where θ_s denotes the granular temperature (Gidaspow, 1994; Jackson, 2000). This equation reads:

$$\rho_s \partial_t [\alpha_s (3/2)\theta_s] = -\rho_s \partial_{\boldsymbol{x}} \cdot \alpha_s (3/2)\theta_s \boldsymbol{u}_s - \partial_{\boldsymbol{x}} \cdot \boldsymbol{q}_s - \boldsymbol{S}_s : \partial_{\boldsymbol{x}} \boldsymbol{u}_s - S_c - S_v + G \tag{2.9}$$

where $\boldsymbol{q}_s$ is the granular heat flux, S_c and S_v are sink terms of granular internal energy generated by inelastic particle collisions and viscous resistance to particle motions, respectively, while G is a source term owing to the generation of particle velocity fluctuations induced by fluctuating fluid–particle forces or any other of the source mechanisms previously mentioned.

As we see, the equations in the Eulerian–Eulerian model contain several undetermined terms. In Section 2.2.1, we discuss how these can be closed. With these closures, the Eulerian–Eulerian model can be used to simulate liquid–particle fluid dynamics. But when the mean variables, e.g., α_e, α_s, $\boldsymbol{u}_e$ and $\boldsymbol{u}_s$, are turbulent, capturing their fluctuations is extremely demanding computationally. To reduce the computational cost, one can operate similarly to what is done for single-phase turbulent flows, Reynolds averaging the equations that govern the evolution of the turbulent variables (here, Eqs. (2.3), (2.4), (2.6), (2.7) and (2.9)).

2.1.2. Reynolds averaging method

With the method outlined by Fox (2014), to which we refer for details, the Reynolds-averaged equations of change can be readily derived; here, we just present these transport equations, referring to them as *Fox model*. This model involves Reynolds averages, fluid averages and solid averages. For a given Eulerian variable ζ, these three averages are respectively denoted as $\langle \zeta \rangle$, $\langle \zeta \rangle_E$ and $\langle \zeta \rangle_S$. The corresponding fluctuating quantities are denoted by ζ', ζ'' and ζ''', respectively. The fluid and solid averages are similar to Favre averages and are related to the Reynolds averages as follows:

$$\langle \zeta \rangle_E \equiv \langle \alpha_e \zeta \rangle / \langle \alpha_e \rangle \quad ; \quad \langle \zeta \rangle_S \equiv \langle \alpha_s \zeta \rangle / \langle \alpha_s \rangle \tag{2.10}$$

So, in these averages the volume fraction has the same role as the fluid density in the Favre averages. For the fluid phase, the Reynolds-averaged continuity and dynamical equations read:

$$\partial_t \langle \alpha_e \rangle = -\partial_{\boldsymbol{x}} \cdot \langle \alpha_e \rangle \langle \boldsymbol{u}_e \rangle_E \tag{2.11}$$

$$\rho_e \partial_t (\langle \alpha_e \rangle \langle \boldsymbol{u}_e \rangle_E) = -\rho_e \partial_{\boldsymbol{x}} \cdot \langle \alpha_e \rangle \langle \boldsymbol{u}_e \rangle_E \langle \boldsymbol{u}_e \rangle_E - \partial_{\boldsymbol{x}} \cdot \langle \boldsymbol{S}_e \rangle - \rho_e \partial_{\boldsymbol{x}} \cdot \langle \alpha_e \rangle \langle \boldsymbol{u}_e'' \boldsymbol{u}_e'' \rangle_E - \langle \boldsymbol{f}_p \rangle + \langle \alpha_e \rangle \rho_e \boldsymbol{g} \tag{2.12}$$

In Eq. (2.12), the term involving $\langle \boldsymbol{u}_e'' \boldsymbol{u}_e'' \rangle_E$ is caused by the turbulence in the Eulerian velocity field of the fluid phase (i.e., it is caused by the fluctuations of $\boldsymbol{u}_e$, and not of the point velocity $\bar{\boldsymbol{u}}_e$) and represents the turbulent stress tensor of the fluid phase, defined by:

$$\boldsymbol{T}_e \equiv \langle \alpha_e \rangle \rho_e \langle \boldsymbol{u}_e'' \boldsymbol{u}_e'' \rangle_E \tag{2.13}$$

For the solid phase, the Reynolds-averaged continuity and dynamical equations – obtained by averaging Eqs. (2.6) and (2.7) – read:

$$\partial_t \langle \alpha_s \rangle = -\partial_{\boldsymbol{x}} \cdot \langle \alpha_s \rangle \langle \boldsymbol{u}_s \rangle_S \tag{2.14}$$

$$\rho_s \partial_t (\langle \alpha_s \rangle \langle \boldsymbol{u}_s \rangle_S) = -\rho_s \partial_{\boldsymbol{x}} \cdot \langle \alpha_s \rangle \langle \boldsymbol{u}_s \rangle_S \langle \boldsymbol{u}_s \rangle_S - \partial_{\boldsymbol{x}} \cdot \langle \boldsymbol{S}_s \rangle - \rho_s \partial_{\boldsymbol{x}} \cdot \langle \alpha_s \rangle \langle \boldsymbol{u}_s''' \boldsymbol{u}_s''' \rangle_S + \langle \boldsymbol{f}_p \rangle + \langle \alpha_s \rangle \rho_s \boldsymbol{g} \tag{2.15}$$

In Eq. (2.15), similarly to the fluid phase, the term involving $\langle \boldsymbol{u}_s''' \boldsymbol{u}_s''' \rangle_S$ is caused by turbulence in the Eulerian solid velocity field and gives rise to the solid-phase turbulent stress tensor:

$$\boldsymbol{T}_s \equiv \langle \alpha_s \rangle \rho_s \langle \boldsymbol{u}_s''' \boldsymbol{u}_s''' \rangle_S \tag{2.16}$$

The Reynolds-averaged balance equation for the granular internal energy of the particulate phase is obtained by averaging Eq. (2.9) and takes the form:

$$\rho_s \partial_t [\langle \alpha_s \rangle (3/2) \langle \theta_s \rangle_S] = -\rho_s \partial_{\boldsymbol{x}} \cdot \langle \alpha_s \rangle (3/2) \langle \theta_s \rangle_S \langle \boldsymbol{u}_s \rangle_S - \rho_s \partial_{\boldsymbol{x}} \cdot \langle \alpha_s \rangle (3/2) \langle \theta_s''' \boldsymbol{u}_s''' \rangle_S - \partial_{\boldsymbol{x}} \cdot \langle \boldsymbol{q}_s \rangle - \langle \boldsymbol{S}_s : \partial_{\boldsymbol{x}} \boldsymbol{u}_s \rangle - \langle S_c \rangle - \langle S_v \rangle + \langle G \rangle \tag{2.17}$$

where $\rho_s \langle \alpha_s \rangle (3/2) \langle \theta_s''' \boldsymbol{u}_s''' \rangle_S$, sometimes equivalently written as $\rho_s \langle \alpha_s \rangle (3/2) \langle \theta_s \boldsymbol{u}_s''' \rangle_S$, is the turbulent flux of granular internal energy induced by fluctuations in θ_s and $\boldsymbol{u}_s$.

As we see, the averaging process introduces several undetermined terms. Details on their closures will be provided in Section 2.2.2.

2.1.3. One-step averaging method

Many turbulent multifluid models reported in the literature have not been derived rigorously by averaging the Eulerian–Eulerian equations of change. We refer to them as *one-step averaging models*. In these models, the balance equations are formally equal to those in the Eulerian–Eulerian models, but the effective stress tensors are interpreted, and therefore closed, differently. For the fluid phase, the term $\alpha_e \rho_e \langle \hat{\boldsymbol{u}} \hat{\boldsymbol{u}} \rangle_e$ featuring in Eq. (2.5) is regarded as the turbulent contribution to the effective stress tensor of the fluid, while the first two terms on the right-hand side of Eq. (2.5) are regarded as the laminar part of the effective stress tensor. Therefore, $\boldsymbol{T}_e$ is confused with $\alpha_e \rho_e \langle \hat{\boldsymbol{u}} \hat{\boldsymbol{u}} \rangle_e$. Furthermore, the fluid–particle interaction force $\langle \boldsymbol{f}_p \rangle$ is confused with $\boldsymbol{f}_p$. This is important, insofar as it might lead to an incorrect closure of these terms. Thus, the linear momentum balance equation is expressed as follows:

$$\rho_e \partial_t (\alpha_e \boldsymbol{u}_e) = -\rho_e \partial_{\boldsymbol{x}} \cdot \alpha_e \boldsymbol{u}_e \boldsymbol{u}_e - \partial_{\boldsymbol{x}} \cdot (\boldsymbol{S}_{e,l} + \boldsymbol{S}_{e,t}) - \boldsymbol{f}_p + \alpha_e \rho_e \boldsymbol{g} \tag{2.18}$$

where $\boldsymbol{S}_{e,l}$ is the laminar part of the effective stress, related to the fluid viscosity, and $\boldsymbol{S}_{e,t}$ is the turbulent part of the effective stress, related to the "fluid velocity fluctuations".

For the solid phase, the dynamical equation is formulated similarly to Eq. (2.18), the solid effective stress tensor also being regarded as

the sum of a laminar part $\boldsymbol{S}_{s,l}$ and a turbulent part $\boldsymbol{S}_{s,t}$. In the works by Enwald et al. (1996) and Peirano and Leckner (1998), $\boldsymbol{S}_{s,l}$ is closed using the kinetic theory of granular flows (KTGF) model, which considers both kinetic stress and collisional stress. In the turbulent part $\boldsymbol{S}_{s,t}$, these authors also accounted for contributions from both kinetic and collisional stresses, modeling them via turbulent closures. But instead of expressing $\boldsymbol{S}_{s,t}$ as a function of the solid-phase turbulent properties, such as the solid turbulent kinetic energy k_s and dissipation rate ε_s, they expressed it in terms of the granular temperature θ_s, since they regarded k_s and θ_s as the same quantity. This led them to consider only the balance equation for the granular internal energy, without solving the transport equations for k_s and ε_s. Nevertheless, θ_s arises from particle velocity fluctuations, whereas k_s arises from fluctuations of the solid Eulerian velocity field $\boldsymbol{u}_s$, making these quantities conceptually distinct. Consequently, this approach seems to be inadequate (Fox, 2014). Moreover, to our knowledge, it has never been used to simulate liquid–particle flows in agitated vessels. Therefore, we will not consider it further.

In another approach used by Wadnerkar et al. (2012, 2016), and Maluta et al. (2019), $\boldsymbol{S}_{s,l}$ again includes a collisional part and a kinetic part related to particle velocity fluctuations, both closed via the KTGF model, but $\boldsymbol{S}_{s,t}$ is expressed in terms of k_s and ε_s. Hence, the balance equations for k_s and ε_s are solved along with that for the granular internal energy. Even if here θ_s and k_s are not confused, this approach still contains some conceptual errors. First, the term representing the total conversion of kinetic energy into granular internal energy is expressed as $\boldsymbol{S}_s : \partial_{\boldsymbol{x}} \boldsymbol{u}_s$, thus featuring the entire solid effective stress tensor; this is incorrect, because it should feature only the laminar part of $\boldsymbol{S}_s$ and it does not account for the deformation work done by the fluctuating part of $\boldsymbol{S}_{s,l}$ on the fluctuating mean velocity field $\boldsymbol{u}_s'''$ (this is discussed further in Section 2.2.2). Second, some terms in the governing equations, including those for the turbulent properties of the fluid and solid phases, which emerge from the Reynolds averaging process (outlined in Section 2.1.2) are overlooked. Despite this, the results of these models, below referred to as *OS models*, agree reasonably well with experimental data of liquid–particle turbulent flows in agitated vessels. This motivates us to explore them further, along with the constitutive equations that they adopt.

2.2. Closure equations

2.2.1. Closures for the Eulerian-Eulerian model

The Eulerian–Eulerian balance equations (Eqs. (2.3), (2.4), (2.6), (2.7) and (2.9)) feature several undetermined terms: the phasic effective stress tensors, the average fluid–particle interaction force, the granular heat flux, and the sink and source terms of granular internal energy. In the literature, various constitutive equations have been proposed for these terms; here we report some commonly-used examples.

For the fluid effective stress tensor, the Newtonian closure is often adopted (see, for instance, Chen et al., 2009; Gidaspow and Huang, 2009; Mazzei et al., 2010; Yilmaz et al., 2011; Kaushal et al., 2012; Wang et al., 2013; Fox, 2014; Oke et al., 2014), given by:

$$\boldsymbol{S}_e = (p_e - \lambda_e \partial_{\boldsymbol{x}} \cdot \boldsymbol{u}_e)\boldsymbol{I} - \eta_e[\dot{\boldsymbol{\gamma}}_e - (2/3)\partial_{\boldsymbol{x}} \cdot \boldsymbol{u}_e \boldsymbol{I}] \tag{2.19}$$

where p_e, λ_e and η_e are the mean pressure, bulk viscosity and viscosity of the fluid, respectively, $\boldsymbol{I}$ is the unit tensor, whilst $\dot{\boldsymbol{\gamma}}_e \equiv \partial_{\boldsymbol{x}} \boldsymbol{u}_e + (\partial_{\boldsymbol{x}} \boldsymbol{u}_e)^{\dagger}$ is twice the deformation rate tensor associated with the mean velocity field of the fluid phase. Then, the problem of closure reduces to finding suitable constitutive expressions for the pressure and the viscosities. If the compressibility of the fluid is neglected, the pressure does not have to be specified constitutively. Furthermore, often it is assumed that $\eta_e = \alpha_e \mu_e$, where μ_e denotes the molecular viscosity of the interstitial fluid, while λ_e is neglected. Owing to their popularity, in this work we will adopt these closures; however, other authors, such as Gidaspow (1994), assume that $\eta_e = \mu_e$. Fox (2014) employs a similar closure, with $\eta_e = \mu_e + \mu_e^{\star}$, where $\mu_e^{\star}$ is a "pseudo-turbulent" viscosity that accounts for the stress arising from the point fluid velocity fluctuations due, for instance, to particle wakes. All these closures seem to neglect the viscosity contribution related to the particle-presence stress ($\boldsymbol{S}_{e,p}$ in Eq. (2.5)); for more details about this aspect, see Jamshidi et al. (2019).

Usually, the solid effective stress tensor is modeled with an equation analogous to Eq. (2.19). Constitutive equations for the granular (or solid) pressure p_s, bulk viscosity λ_s and viscosity η_s derived from the kinetic theory of granular flows are generally employed, unless the suspension is extremely dense (that is, close to the packing limit). In simulations of liquid–particle flows in agitated vessels, the closures of Syamlal et al. (1993) and Gidaspow (1994) are generally used (Wadnerkar et al., 2016; Maluta et al., 2019; Kazemzadeh et al., 2020). We should note that, originally, these closures were obtained without considering the presence of the interstitial fluid. In this study, we adopt the model proposed by Syamlal et al. (1993). In it, the solid pressure, bulk viscosity and viscosity are closed as follows:

$$p_s = \alpha_s \rho_s \theta_s + 2\alpha_s^2 \rho_s \theta_s g_0 (1+e) \quad ; \quad \lambda_s = (4/3)\alpha_s^2 \rho_s d_p g_0 (1+e)\sqrt{\theta_s/\pi}$$
$$\eta_s = \frac{\alpha_s \rho_s d_p \sqrt{\theta_s \pi}}{6(3-e)}\left[1 + \frac{2}{5}\alpha_s g_0 (1+e)(3e-1)\right] + (3/5)\lambda_s \tag{2.20}$$

where e is the restitution coefficient (equal to unity if the particle collisions are elastic) and g_0 is the radial distribution function, given by:

$$g_0 = \left[1 - (\alpha_s/\alpha_{s,max})^{1/3}\right]^{-1} \tag{2.21}$$

where $\alpha_{s,max}$ is the maximum value of the solid volume fraction. The solid pressure and viscosities depend on the granular temperature, so the balance equation for the granular internal energy, Eq. (2.9), must be solved. In it, Syamlal et al. (1993) express the granular heat flux as follows:

$$\boldsymbol{q}_s = -k_\theta \partial_{\boldsymbol{x}} \theta_s \tag{2.22}$$

with:

$$k_\theta = \frac{15\alpha_s \rho_s d_p \sqrt{\theta_s \pi}}{4(41-33\zeta)}\left\{1 + \left[\frac{12}{5}\zeta^2(4\zeta - 3) + \frac{16}{15\pi}\zeta(41 - 33\zeta)\right]\alpha_s g_0\right\} \tag{2.23}$$

where k_θ is the granular conductivity and $\zeta \equiv (1+e)/2$. Syamlal et al. (1993) neglect the source term G, as it is quite often done. The closures for the sink terms related to inelastic collisions and to viscous resistance to the particle motions read:

$$S_c = \frac{\alpha_s \rho_s \theta_s (1-e^2)}{2\tau_s^c} \quad ; \quad \tau_s^c \equiv \frac{d_p}{24\alpha_s g_0}\sqrt{\frac{\pi}{\theta_s}} \quad ; \quad S_v = 3\beta\theta_s \tag{2.24}$$

where τ_s^c is the characteristic time scale of particle collisions and β is the drag coefficient, whose closure is discussed below.

The mean fluid–particle interaction force $\boldsymbol{f}_p$ comprises several contributors, the primary ones being the buoyancy force $\boldsymbol{f}_{p,B}$, the drag force $\boldsymbol{f}_{p,D}$, the lift force $\boldsymbol{f}_{p,L}$ and the virtual mass force $\boldsymbol{f}_{p,V}$. In simulations of liquid–particle flows in agitated vessels, the last two are usually negligible (Ljungqvist and Rasmuson, 2001; Shan et al., 2008; Wadnerkar et al., 2012; Tamburini et al., 2014; Wadnerkar et al., 2016). Hence, we will not consider them. For the buoyancy force, various definitions may be adopted (for details, see Jackson, 2000), the most common one regarding the force as proportional to the gradient of the mean fluid pressure (Foscolo et al., 1983; Gibb, 1991; Astarita, 1993; Di Felice, 1994; Gibilaro, 2001), the proportionality constant being the solid volume fraction. The drag force is instead always proportional to the slip velocity between the two phases, the proportionality constant being the drag coefficient. Therefore, we have:

$$\boldsymbol{f}_{p,B} \equiv -\alpha_s \partial_{\boldsymbol{x}} p_e \quad ; \quad \boldsymbol{f}_{p,D} \equiv \beta(\boldsymbol{u}_e - \boldsymbol{u}_s) \tag{2.25}$$

Several closures are available for the drag coefficient β. For instance, see Jackson (2000), Mazzei and Lettieri (2007) and Marchisio and Fox

(2013) for reviews. Here, we consider those of Huilin et al. (2003) and Syamlal et al. (1993), which are often employed in the literature. We will refer to them as Huilin–Gidaspow (HG) and Syamlal–O'Brien (SB) models. The first combines the closures of Wen and Yu (1966) and Ergun (1952), with a smooth transition from the former (prevailing at low α_s values) to the latter around a solid volume fraction of 0.2. The closure is given by:

$$\beta = f\beta_E + (1-f)\beta_{WY} \tag{2.26}$$

where:

$$f = \frac{1}{2} + \frac{\arctan[262.5(\alpha_s - 0.2)]}{\pi} \quad ; \quad \beta_E = 150\frac{\alpha_s^2\mu_e}{\alpha_e d_p^2} + 1.75\frac{\alpha_s\rho_e}{d_p}|\boldsymbol{u}_e - \boldsymbol{u}_s|$$

$$\beta_{WY} = \frac{3}{4}C_D\frac{\rho_e|\boldsymbol{u}_e - \boldsymbol{u}_s|\alpha_s}{d_p}\alpha_e^{-1.65}$$

$$C_D = \begin{cases} 24(1+0.15\mathrm{Re}^{0.687})/\mathrm{Re} & \text{for } \mathrm{Re} < 1000 \\ 0.44 & \text{for } \mathrm{Re} \geq 1000 \end{cases} \quad ; \quad \mathrm{Re} \equiv \frac{\alpha_e\rho_e|\boldsymbol{u}_e - \boldsymbol{u}_s|d_p}{\mu_e} \tag{2.27}$$

The SB model reads:

$$\beta = \frac{3}{4}C_D\frac{\alpha_s\alpha_e\rho_e}{\xi^2 d_p}|\boldsymbol{u}_e - \boldsymbol{u}_s| \tag{2.28}$$

where:

$$C_D = \left(0.63 + \frac{4.8}{\sqrt{\Psi/\xi}}\right)^2 \quad ; \quad \xi = \frac{1}{2}\left[A - 0.06\Psi + \sqrt{(0.06\Psi)^2 + 0.12(2B-A)\Psi + A^2}\right]$$

$$\Psi = \mathrm{Re}/\alpha_e \quad ; \quad A = \alpha_e^{4.14} \quad ; \quad B = \begin{cases} 0.8\alpha_e^{1.28} & \text{for } \alpha_e \leq 0.85 \\ \alpha_e^{2.65} & \text{for } \alpha_e > 0.85 \end{cases} \tag{2.29}$$

The expressions reported above are consistent with the buoyancy force definition given in Eq. (2.25)A. Other definitions require modified expressions (Mazzei, 2019).

2.2.2. Closures for the fox model

In this section, we present the closures for the undetermined terms featuring in the Fox model. Most of the expressions given below are consistent with those found in Fox (2014), to whom we refer for mathematical details; however, the notation and, more importantly, some constitutive equations are different. For instance, Fox assumes $\alpha_s\rho_s/\beta$ (i.e., the drag time scale) to be a constant, while we do not; in addition, as mentioned, the author uses the closure $\eta_e = \mu_e + \mu_e^\star$, while we adopt the expression $\eta_e = \alpha_e\mu_e$, since this is the closure adopted in most versions of the OS model.

Reynolds averaging Eq. (2.19), with $\lambda_e = 0$ and $\eta_e = \alpha_e\mu_e$, yields:

$$\langle \boldsymbol{S}_e\rangle \approx \langle p_e\rangle \boldsymbol{I} - \langle\alpha_e\rangle\mu_e[\partial_{\boldsymbol{x}}\langle\boldsymbol{u}_e\rangle_E + (\partial_{\boldsymbol{x}}\langle\boldsymbol{u}_e\rangle_E)^\dagger - (2/3)\partial_{\boldsymbol{x}}\cdot\langle\boldsymbol{u}_e\rangle_E\boldsymbol{I}] \tag{2.30}$$

This expression is not rigorous, because it neglects contributions related to $\boldsymbol{u}_e''$, that is, to the fluctuations of the fluid Eulerian velocity $\boldsymbol{u}_e$. For details about the validity (and the limitations) of this approximation, we refer to Fox (2014). The Reynolds average of $\boldsymbol{S}_s$ is approximated as:

$$\begin{aligned}\langle \boldsymbol{S}_s\rangle &= [\langle p_s\rangle - \langle\lambda_s\partial_{\boldsymbol{x}}\cdot\boldsymbol{u}_s\rangle]\boldsymbol{I} - \langle\eta_s[\dot{\boldsymbol{\gamma}}_s - (2/3)\partial_{\boldsymbol{x}}\cdot\boldsymbol{u}_s\boldsymbol{I}]\rangle \\ &\approx \boldsymbol{S}_s(\langle\alpha_s\rangle,\langle\theta_s\rangle_S,\langle\boldsymbol{u}_s\rangle_S) = [p_s(\langle\alpha_s\rangle,\langle\theta_s\rangle_S) - \lambda_s(\langle\alpha_s\rangle,\langle\theta_s\rangle_S)\partial_{\boldsymbol{x}}\cdot\langle\boldsymbol{u}_s\rangle_S]\boldsymbol{I} \\ &- \eta_s(\langle\alpha_s\rangle,\langle\theta_s\rangle_S)[\partial_{\boldsymbol{x}}\langle\boldsymbol{u}_s\rangle_S + (\partial_{\boldsymbol{x}}\langle\boldsymbol{u}_s\rangle_S)^\dagger - (2/3)\partial_{\boldsymbol{x}}\cdot\langle\boldsymbol{u}_s\rangle_S\boldsymbol{I}]\end{aligned} \tag{2.31}$$

where $p_s(\langle\alpha_s\rangle,\langle\theta_s\rangle_S)$, $\lambda_s(\langle\alpha_s\rangle,\langle\theta_s\rangle_S)$ and $\eta_s(\langle\alpha_s\rangle,\langle\theta_s\rangle_S)$ are calculated by Eqs. (2.20), but with α_s and θ_s replaced by $\langle\alpha_s\rangle$ and $\langle\theta_s\rangle_S$, respectively.

The turbulent stress tensor of the fluid phase $\boldsymbol{T}_e$ (Eq. (2.13)) can be closed adopting the Boussinesq eddy viscosity hypothesis, given by:

$$\boldsymbol{T}_e = (2/3)\langle\alpha_e\rangle\rho_e k_e\boldsymbol{I} - \langle\alpha_e\rangle\mu_{t,e}[\partial_{\boldsymbol{x}}\langle\boldsymbol{u}_e\rangle_E + (\partial_{\boldsymbol{x}}\langle\boldsymbol{u}_e\rangle_E)^\dagger - (2/3)\partial_{\boldsymbol{x}}\cdot\langle\boldsymbol{u}_e\rangle_E\boldsymbol{I}] \tag{2.32}$$

where k_e and $\mu_{t,e}$ are the turbulent kinetic energy and the turbulent viscosity of the fluid phase, respectively. The latter is given by:

$$\mu_{t,e} = C_{\mu e}\rho_e k_e^2/\varepsilon_e \tag{2.33}$$

where ε_e is the dissipation rate of the fluid turbulent kinetic energy. $C_{\mu e}$ is a parameter, usually set equal to 0.09 (Wilcox, 1998; Shan et al., 2008; Riella et al., 2018). The solid turbulent stress tensor $\boldsymbol{T}_s$ (Eq. (2.16)) is modeled with equations analogous to Eqs. (2.32) and (2.33), with k_s representing the turbulent kinetic energy of the solid phase and ε_s its dissipation rate. Note that:

$$k_e \equiv \frac{1}{2}\langle\boldsymbol{u}_e''\cdot\boldsymbol{u}_e''\rangle_E \quad ; \quad k_s \equiv \frac{1}{2}\langle\boldsymbol{u}_s'''\cdot\boldsymbol{u}_s'''\rangle_S \tag{2.34}$$

Therefore, k_e and k_s are related to the fluctuations of the Eulerian velocities of the fluid and solid phases ($\boldsymbol{u}_e$ and $\boldsymbol{u}_s$), respectively. This clearly reveals that k_s is distinct from θ_s, which is instead related to the particle velocity fluctuations, $\hat{\boldsymbol{u}}_s \equiv \bar{\boldsymbol{u}}_s - \boldsymbol{u}_s$.

Then, we focus on the Reynolds average of the mean fluid–particle interaction force. As discussed, here we only consider the buoyancy and drag forces. Using Eq. (2.25)A, we obtain:

$$\langle\boldsymbol{f}_{p,B}\rangle = -\langle\alpha_s\rangle\partial_{\boldsymbol{x}}\langle p_e\rangle - \langle\alpha_s'\partial_{\boldsymbol{x}}p_e'\rangle \tag{2.35}$$

Here, the covariance of the fluctuations of the solid phase volume fraction and the gradient of the fluid mean pressure is closed by:

$$\langle\alpha_s'\partial_{\boldsymbol{x}}p_e'\rangle = C_p\langle\alpha_e\rangle\langle\alpha_s\rangle(\rho_s - \rho_e)\boldsymbol{g} \tag{2.36}$$

where C_p ranges from zero to unity (Fox, 2014). For the drag force, we approximate the Reynolds average of Eq. (2.25)B with the following expression:

$$\langle\boldsymbol{f}_{p,D}\rangle = \beta(\langle\alpha_s\rangle,\langle\boldsymbol{u}_e\rangle_E,\langle\boldsymbol{u}_s\rangle_S)\left[(\langle\boldsymbol{u}_e\rangle_E - \langle\boldsymbol{u}_s\rangle_S) + \boldsymbol{u}_{dr}\right] \tag{2.37}$$

with:

$$\boldsymbol{u}_{dr} \equiv \frac{\langle\alpha_s'\boldsymbol{u}_e''\rangle}{\langle\alpha_e\rangle\langle\alpha_s\rangle} \tag{2.38}$$

Here, $\beta(\langle\alpha_s\rangle,\langle\boldsymbol{u}_e\rangle_E,\langle\boldsymbol{u}_s\rangle_S)$ is calculated by Eqs. (2.26) and (2.27) or Eqs. (2.28) and (2.29) replacing the Eulerian variables with their corresponding Reynolds or phase averages. In Eq. (2.37), the part of $\langle\boldsymbol{f}_{p,D}\rangle$ related to $\boldsymbol{u}_{dr}$ is referred to as *turbulent dispersion force*, while $\boldsymbol{u}_{dr}$ is referred to as *drift velocity*. Fox (2014) closes this velocity as follows:

$$\boldsymbol{u}_{dr} = -\frac{\mu_{e,t}}{\langle\alpha_e\rangle\langle\alpha_s\rangle\rho_e\mathrm{Sc}_{es}}\partial_{\boldsymbol{x}}\langle\alpha_s\rangle - C_g(\langle\boldsymbol{u}_e\rangle_E - \langle\boldsymbol{u}_s\rangle_S) \quad ; \quad \mathrm{Sc}_{es} \equiv (k_e/k_s)^{1/2} \tag{2.39}$$

Here, Sc_{es} is a turbulent Schmidt number and $0 \leq C_g \leq 1$. Note that as indicated by Fox (2014), the second term on the right-hand side of Eq. (2.39)A is obtained exclusively for cases where $\rho_e \lll \rho_s$; for liquid–particle systems, this term may have to be modeled differently.

Now, we provide the closures for the undetermined terms in the Reynolds-averaged balance equation for the granular internal energy (Eq. (2.17)). As it is often done, $\langle G\rangle$ is neglected. The turbulent granular internal energy flux $\langle\theta_s'''\boldsymbol{u}_s'''\rangle_S$ is modeled via the gradient diffusion model, writing:

$$\langle\theta_s'''\boldsymbol{u}_s'''\rangle_S = -\frac{\mu_{t,s}}{\rho_s\mathrm{Pr}_{es}}\partial_{\boldsymbol{x}}\langle\theta_s\rangle_S \tag{2.40}$$

Here, Pr_{es} is the turbulent Prandtl number, whose value ranges from 0.5 to 0.9 (Wilcox, 1998); in this study we take it to be 0.85. $\langle\boldsymbol{q}_s\rangle$, $\langle S_c\rangle$ and $\langle S_v\rangle$ are approximated as:

$$\begin{aligned}\langle\boldsymbol{q}_s\rangle &= -\langle k_\theta\partial_{\boldsymbol{x}}\theta_s\rangle \approx -k_\theta(\langle\alpha_s\rangle,\langle\theta_s\rangle_S)\partial_{\boldsymbol{x}}\langle\theta_s\rangle_S \\ \langle S_c\rangle &\approx S_c(\langle\alpha_s\rangle,\langle\theta_s\rangle_S) \quad ; \quad \langle S_v\rangle = 3\langle\beta\theta_s\rangle \approx 3\beta(\langle\alpha_s\rangle,\langle\boldsymbol{u}_e\rangle_E,\langle\boldsymbol{u}_s\rangle_S)\langle\theta_s\rangle_S\end{aligned} \tag{2.41}$$

where $k_\theta(\langle\alpha_s\rangle,\langle\theta_s\rangle_S)$ and $S_c(\langle\alpha_s\rangle,\langle\theta_s\rangle_S)$ are calculated by Eqs. (2.23) and (2.24), respectively, substituting α_s and θ_s with their Reynolds and solid-phase averages, respectively. The fourth term on the right-hand side of Eq. (2.17) can be approximately expressed as follows:

$$\langle \boldsymbol{S}_s : \partial_{\boldsymbol{x}} \boldsymbol{u}_s \rangle = \langle \alpha_s \rangle \langle (\boldsymbol{S}_s/\alpha_s) : \partial_{\boldsymbol{x}} \boldsymbol{u}_s \rangle_S$$
$$\approx \boldsymbol{S}_s(\langle \alpha_s \rangle, \langle \theta_s \rangle_S) : \partial_{\boldsymbol{x}} \langle \boldsymbol{u}_s \rangle_S + \langle \alpha_s \rangle \langle (\boldsymbol{S}_s/\alpha_s) : \partial_{\boldsymbol{x}} \boldsymbol{u}_s''' \rangle_S \quad (2.42)$$

As seen, the second part accounts for the deformation work done by $\boldsymbol{S}_s/\alpha_s$ on the fluctuating mean velocity field $\boldsymbol{u}_s'''$. It quantifies the conversion of solid turbulent kinetic energy into granular internal energy (this term features in the solid turbulent kinetic energy balance equation with opposite sign). The dominant part of this quantity represents the production of granular internal energy due to the (irreversible) dissipation of the solid turbulent kinetic energy and is closed as $\langle \alpha_s \rangle \rho_s \varepsilon_s$. Thus, we have:

$$\langle \alpha_s \rangle \langle (\boldsymbol{S}_s/\alpha_s) : \partial_{\boldsymbol{x}} \boldsymbol{u}_s''' \rangle_S = \langle p_s \partial_{\boldsymbol{x}} \cdot \boldsymbol{u}_s''' \rangle - \langle \alpha_s \rangle \rho_s \varepsilon_s \quad (2.43)$$

Using Eq. (2.20)A, we can express the first term on the right-hand side in terms on granular temperature. This shows that, for non-dense suspensions, $\langle p_s \partial_{\boldsymbol{x}} \cdot \boldsymbol{u}_s''' \rangle$ is related to the covariance of the fluctuations in granular temperature and dilatation. This term is usually neglected, insofar as θ_s''' is an integral-scale quantity, while $\partial_{\boldsymbol{x}} \cdot \boldsymbol{u}_s'''$ is a small-scale quantity, and so they should be uncorrelated (Wilcox, 1998). Even if for multiphase systems this argument has not been verified, we accept it and neglect this contribution.

The closures reported above require knowledge of the turbulent kinetic energy and of its dissipation rate for both phases (e.g., refer to Eqs. (2.33), (2.39) and (2.43)). To obtain these fields, we have to solve their transport equations. For the fluid turbulent kinetic energy, the equation reads:

$$\rho_e \partial_t (\langle \alpha_e \rangle k_e) = -\rho_e \partial_{\boldsymbol{x}} \cdot \langle \alpha_e \rangle k_e \langle \boldsymbol{u}_e \rangle_E + \partial_{\boldsymbol{x}} \cdot \langle \alpha_e \rangle \left(\mu_e + \frac{\mu_{t,e}}{\sigma_{e,k}} \right) \partial_{\boldsymbol{x}} k_e$$
$$- \boldsymbol{T}_e : \partial_{\boldsymbol{x}} \langle \boldsymbol{u}_e \rangle_E - \langle \alpha_e \rangle \rho_e \varepsilon_e + \Pi_{k,e} + \Pi_{k,ep} + \Pi_{k,e\rho} \quad (2.44)$$

Here, $\sigma_{e,k}$ is a constant, assigned to be unity (Wilcox, 1998). $\Pi_{k,e}$, $\Pi_{k,ep}$ and $\Pi_{k,e\rho}$ are the source terms due to the turbulent interaction between the phases, the gradient of the Reynolds-averaged fluid pressure, and the covariance of the fluctuations of the Eulerian fluid velocity and fluid pressure gradient, respectively. Their closures are given by Fox (2014) and read:

$$\Pi_{k,e} = \beta(\langle \alpha_s \rangle, \langle \boldsymbol{u}_e \rangle_E, \langle \boldsymbol{u}_s \rangle_S)\{2[\Psi_k (k_e k_s)^{1/2} - k_e] - \boldsymbol{u}_{dr} \cdot (\langle \boldsymbol{u}_e \rangle_E - \langle \boldsymbol{u}_s \rangle_S)\}$$
$$\Pi_{k,ep} = \langle \alpha_s \rangle \boldsymbol{u}_{dr} \cdot \partial_{\boldsymbol{x}} \langle p_e \rangle \quad ; \quad \Pi_{k,e\rho} = C_\rho \langle \alpha_s \rangle (\rho_s - \rho_e) \boldsymbol{u}_{dr} \cdot \boldsymbol{g} \quad (2.45)$$

Here, Ψ_k and C_ρ are constants, taken to be unity (Riella et al., 2018). Notice that, following Rumsey (2010), on the right-hand side of Eq. (2.44) we have neglected the pressure–dilatation term $\langle p_e \partial_{\boldsymbol{x}} \cdot \boldsymbol{u}_e'' \rangle$. The transport equations for the fluid turbulent kinetic energy dissipation rate reads:

$$\rho_e \partial_t (\langle \alpha_e \rangle \varepsilon_e) = -\rho_e \partial_{\boldsymbol{x}} \cdot \langle \alpha_e \rangle \varepsilon_e \langle \boldsymbol{u}_e \rangle_E + \partial_{\boldsymbol{x}} \cdot \langle \alpha_e \rangle \left(\mu_e + \frac{\mu_{t,e}}{\sigma_{e,\varepsilon}} \right) \partial_{\boldsymbol{x}} \varepsilon_e$$
$$- \frac{\varepsilon_e}{k_e} (C_1 \boldsymbol{T}_e : \partial_{\boldsymbol{x}} \langle \boldsymbol{u}_e \rangle_E + C_2 \langle \alpha_e \rangle \rho_e \varepsilon_e) + \Pi_{\varepsilon,e} + \frac{\varepsilon_s}{k_s} (C_4 \Pi_{k,ep} + C_5 \Pi_{k,e\rho}) \quad (2.46)$$

where:

$$\Pi_{\varepsilon,e} = \beta(\langle \alpha_s \rangle, \langle \boldsymbol{u}_e \rangle_E, \langle \boldsymbol{u}_s \rangle_S) \left\{ 2C_3 [\Psi_\varepsilon (\varepsilon_e \varepsilon_s)^{1/2} - \varepsilon_e] - C_4 \frac{\varepsilon_s}{k_s} \boldsymbol{u}_{dr} \cdot (\langle \boldsymbol{u}_e \rangle_E - \langle \boldsymbol{u}_s \rangle_S) \right\} \quad (2.47)$$

is a source term owing to the turbulent interaction between the phases. C_1 to C_5, $\sigma_{e,\varepsilon}$ and Ψ_ε are constants. C_1 and C_2 are taken to be 1.44 and 1.92, respectively, $\sigma_{e,\varepsilon}$ is taken to be 1.3 (Wilcox, 1998), whilst the other four constants are taken to be unity (Riella et al., 2018).

The transport equation for the solid turbulent kinetic energy, where, consistently with the approximation used for Eq. (2.43), the pressure–dilatation term $\langle p_s \partial_{\boldsymbol{x}} \cdot \boldsymbol{u}_s''' \rangle$ is neglected, reads:

$$\rho_s \partial_t (\langle \alpha_s \rangle k_s) = -\rho_s \partial_{\boldsymbol{x}} \cdot \langle \alpha_s \rangle k_s \langle \boldsymbol{u}_s \rangle_S + \partial_{\boldsymbol{x}} \cdot \left[\eta_s(\langle \alpha_s \rangle, \langle \theta_s \rangle_S) + \frac{\langle \alpha_s \rangle \mu_{t,s}}{\sigma_{s,k}} \right] \partial_{\boldsymbol{x}} k_s$$
$$- \boldsymbol{T}_s : \partial_{\boldsymbol{x}} \langle \boldsymbol{u}_s \rangle_S - \langle \alpha_s \rangle \rho_s \varepsilon_s + \Pi_{k,s} + \Pi_{k,s\rho} \quad (2.48)$$

Here, $\sigma_{s,k}$ is set to unity (Wilcox, 1998). $\Pi_{k,s}$ and $\Pi_{k,s\rho}$ are source terms owing to the turbulent interaction between the two phases and the covariance of the fluctuations of the Eulerian solid velocity and fluid pressure gradient, respectively. Their closures are:

$$\Pi_{k,s} = 2\beta(\langle \alpha_s \rangle, \langle \boldsymbol{u}_e \rangle_E, \langle \boldsymbol{u}_s \rangle_S)[\Psi_k (k_e k_s)^{1/2} - k_s]$$
$$\Pi_{k,s\rho} = -C_\rho C_p \langle \alpha_e \rangle \langle \alpha_s \rangle (\rho_s - \rho_e)(\langle \boldsymbol{u}_e \rangle_E - \langle \boldsymbol{u}_s \rangle_S) \cdot \boldsymbol{g} - \Pi_{k,e\rho} \quad (2.49)$$

The fourth term on the right-hand side of Eq. (2.48) quantifies the dissipation rate of the solid turbulent kinetic energy and appears in the Reynolds-averaged granular internal energy balance equation with opposite sign. The transport equation for the solid turbulent kinetic energy dissipation rate reads:

$$\rho_s \partial_t (\langle \alpha_s \rangle \varepsilon_s) = -\rho_s \partial_{\boldsymbol{x}} \cdot \langle \alpha_s \rangle \varepsilon_s \langle \boldsymbol{u}_s \rangle_S + \partial_{\boldsymbol{x}} \cdot \left[\eta_s(\langle \alpha_s \rangle, \langle \theta_s \rangle_S) + \frac{\langle \alpha_s \rangle \mu_{t,s}}{\sigma_{s,\varepsilon}} \right] \partial_{\boldsymbol{x}} \varepsilon_s$$
$$- \frac{\varepsilon_s}{k_s} (C_1 \boldsymbol{T}_s : \partial_{\boldsymbol{x}} \langle \boldsymbol{u}_s \rangle_S + C_2 \langle \alpha_s \rangle \rho_s \varepsilon_s) + \Pi_{\varepsilon,s} + C_5 \frac{\varepsilon_s}{k_s} \Pi_{k,s\rho} \quad (2.50)$$

The value of the constant $\sigma_{s,\varepsilon}$ is taken to be 1.3 (Wilcox, 1998), and $\Pi_{\varepsilon,s}$, caused by the turbulent interaction between the phases, is given by:

$$\Pi_{\varepsilon,s} = 2C_3 \beta(\langle \alpha_s \rangle, \langle \boldsymbol{u}_e \rangle_E, \langle \boldsymbol{u}_s \rangle_S)[\Psi_\varepsilon (\varepsilon_e \varepsilon_s)^{1/2} - \varepsilon_s] \quad (2.51)$$

2.2.3. Closures for the OS model

Here, we present the closures for the undetermined terms in the OS model. The laminar stress tensors for the fluid and solid phases, $\boldsymbol{S}_{e,l}$ and $\boldsymbol{S}_{s,l}$, are closed employing Eq. (2.19), with the solid phase properties given by Eqs. (2.20). The turbulent stress tensors for the two phases, $\boldsymbol{S}_{e,t}$ and $\boldsymbol{S}_{s,t}$, are calculated using the Boussinesq eddy viscosity hypothesis, given for the fluid by Eqs. (2.32) and (2.33) (analogous equations hold for the solid), with the Reynolds and phase averages replaced by the Eulerian variables (e.g., $\langle \boldsymbol{u}_e \rangle_E$ is replaced by $\boldsymbol{u}_e$). For the mean fluid–particle interaction force, in addition to the buoyancy force and the drag force calculated using Eq. (2.25), a turbulent dispersion force is directly introduced, given by:

$$\boldsymbol{f}_{p,TD} = \beta \boldsymbol{u}_{dr} \quad (2.52)$$

Alternative closures for the drift velocity distinct from Eq. (2.39) have been employed. One model, proposed by Burns et al. (2004), is given by:

$$\boldsymbol{u}_{dr} = -\frac{\mu_{e,t}}{\alpha_e \alpha_s \rho_e \mathrm{Pr}_{es}} \partial_{\boldsymbol{x}} \alpha_s \quad (2.53)$$

As we can see, if Sc_{es} replaces Pr_{es}, this model reduces to the first term on the right-hand side of Eq. (2.39)A. Another model, by Simonin and Viollet (1990), reads:

$$\boldsymbol{u}_{dr} = -\frac{C_{p,TD}}{\mathrm{Pr}_{es}} \left(\frac{\eta_s}{\alpha_s^2 \rho_s} + \frac{\eta_e}{\alpha_e^2 \rho_e} \right) \partial_{\boldsymbol{x}} \alpha_s \quad (2.54)$$

where $C_{p,TD}$ is an adjustable parameter, which should be calibrated but that usually, for lack of data, is taken to be equal to unity. In this work, we have conformed to this custom.

In the balance equation for the granular internal energy (Eq. (2.9)), G is neglected, while k_θ, S_c and S_v are closed by Eq. (2.22) through Eq. (2.24). Thus, the term involving the turbulent flux of granular internal energy is neglected; furthermore, as said, this approach incorrectly models the production of granular internal energy due to the deformation work (i.e., the third term on the right-hand side of Eq. (2.9)), first because it features $\boldsymbol{S}_s$ instead of $\boldsymbol{S}_{s,l}$, and second because it neglects the deformation work done by the fluctuating part of $\boldsymbol{S}_{s,l}$ on the fluctuating mean velocity field $\boldsymbol{u}_s'''$, i.e., the term $\langle \alpha_s \rangle \langle (\boldsymbol{S}_s/\alpha_s) : \partial_{\boldsymbol{x}} \boldsymbol{u}_s''' \rangle_S$ in Eq. (2.42).

The turbulent properties, e.g., the turbulent kinetic energy, its dissipation rate, and the turbulent viscosity, are generally calculated using

$k-\varepsilon$ models, including the $k-\varepsilon$ per phase model, the $k-\varepsilon$ dispersed model, and the $k-\varepsilon$ mixture model. The $k-\varepsilon$ dispersed model holds only for dilute suspensions, while the mixture model version is suitable for suspensions that can be modeled as an effective fluid, and for which the mixture modeling approach holds (Jackson, 2000; Jamshidi et al., 2019); in this case, the fluid and solid phases share the same turbulent properties as the mixture (e.g., $k_m = k_s = k_e$, where k_m is the turbulent kinetic energy of the mixture). Conversely, the $k-\varepsilon$ per phase model is more broadly applicable, and its transport equations resemble those of the Fox model. Thus, here we adopt this model. For the fluid phase, the transport equation of the turbulent kinetic energy reads:

$$\rho_e \partial_t(\alpha_e k_e) = -\rho_e \partial_{\boldsymbol{x}} \cdot \alpha_e k_e \boldsymbol{u}_e + \partial_{\boldsymbol{x}} \cdot \alpha_e \left(\mu_e + \frac{\mu_{t,e}}{\sigma_{e,k}}\right) \partial_{\boldsymbol{x}} k_e - \boldsymbol{S}_{e,t} : \partial_{\boldsymbol{x}} \boldsymbol{u}_e - \alpha_e \rho_e \varepsilon_e + \Pi_{k,e} \tag{2.55}$$

with $\mu_{t,e}$ given by Eq. (2.33). As in Eq. (2.44), $\Pi_{k,e}$ accounts for the turbulent interaction between the phases; it is generally closed via the Simonin et al. (1990) model:

$$\Pi_{k,e} = -\alpha_e \beta \boldsymbol{u}_{dr} \cdot (\boldsymbol{u}_e - \boldsymbol{u}_s) \tag{2.56}$$

where $\boldsymbol{u}_{dr}$ is closed with Eq. (2.53) or (2.54). Note that Eq. (2.55) does not account for the terms $\Pi_{k,ep}$ and $\Pi_{k,e\rho}$, which feature in Eq. (2.44). The transport equation for k_s is similar and reads:

$$\rho_s \partial_t(\alpha_s k_s) = -\rho_s \partial_{\boldsymbol{x}} \cdot \alpha_s k_s \boldsymbol{u}_s + \partial_{\boldsymbol{x}} \cdot \left(\eta_s + \frac{\alpha_s \mu_{t,s}}{\sigma_{s,k}}\right) \partial_{\boldsymbol{x}} k_s - \boldsymbol{S}_{s,t} : \partial_{\boldsymbol{x}} \boldsymbol{u}_s - \alpha_s \rho_s \varepsilon_s + \Pi_{k,s} \tag{2.57}$$

with:

$$\Pi_{k,s} = -\alpha_s \beta \boldsymbol{u}_{dr} \cdot (\boldsymbol{u}_e - \boldsymbol{u}_s) \tag{2.58}$$

Finally, the transport equations for ε_e and ε_s read:

$$\begin{aligned}\rho_e \partial_t(\alpha_e \varepsilon_e) = &-\rho_e \partial_{\boldsymbol{x}} \cdot \alpha_e \varepsilon_e \boldsymbol{u}_e + \partial_{\boldsymbol{x}} \cdot \alpha_e \left(\mu_e + \frac{\mu_{t,e}}{\sigma_{e,\varepsilon}}\right) \partial_{\boldsymbol{x}} \varepsilon_e \\ &- \frac{\varepsilon_e}{k_e}(C_1 \boldsymbol{S}_{e,t} : \partial_{\boldsymbol{x}} \boldsymbol{u}_e + C_2 \alpha_e \rho_e \varepsilon_e) + \Pi_{\varepsilon,e}\end{aligned} \tag{2.59}$$

$$\begin{aligned}\rho_s \partial_t(\alpha_s \varepsilon_s) = &-\rho_s \partial_{\boldsymbol{x}} \cdot \alpha_s \varepsilon_s \boldsymbol{u}_s + \partial_{\boldsymbol{x}} \cdot \left(\eta_s + \frac{\alpha_s \mu_{t,s}}{\sigma_{s,k}}\right) \partial_{\boldsymbol{x}} \varepsilon_s \\ &- \frac{\varepsilon_s}{k_s}(C_1 \boldsymbol{S}_{s,t} : \partial_{\boldsymbol{x}} \boldsymbol{u}_s + C_2 \alpha_s \rho_s \varepsilon_s) + \Pi_{\varepsilon,s}\end{aligned} \tag{2.60}$$

with:

$$\Pi_{\varepsilon,e} = C_3 \frac{\varepsilon_e}{k_e} \Pi_{k,e} \quad ; \quad \Pi_{\varepsilon,s} = C_3 \frac{\varepsilon_s}{k_s} \Pi_{k,s} \tag{2.61}$$

where the closures for these source terms, related to the turbulent interaction between the phases, have been also advanced by Simonin et al. (1990).

3. Methodology

We have presented the balance equations and the closures for the Fox and OS models. The Fox model, based on the Reynolds averaging method, is theoretically robust, and so it should yield good results for multiphase turbulent flows, and in particular for liquid–particle turbulent flows in agitated vessels — provided appropriate closures are adopted. In contrast, the OS model is unjustified theoretically, but it is widely applied and often gives satisfactory results. This motivates our work, which aims to clarify the reason for this by comparing the results of the two models, assessing them against experimental data, and by evaluating the importance of key terms featuring (or being neglected) in their balance equations.

3.1. Analysis of the models

To facilitate the comparison between the two models, in the Supplementary Information we have written the balance equations in closed form, directly including the closures presented in Section 2.2. In these equations, if in the OS model the Eulerian variables are replaced with their corresponding Reynolds and phase averages, the resulting equations are similar to those in the Fox model. But the latter does feature additional terms. For instance, the Reynolds-averaged dynamical equations contain source terms related to the buoyancy force and arising from the covariance of the fluctuations of the solid phase volume fraction and the gradient of the fluid mean pressure (Eqs. (2.35) and (2.36)). Moreover, as discussed, the Reynolds-averaged granular internal energy balance equation features a turbulent convective term and a source term related to the dissipation of turbulent kinetic energy, while the balance equations for the turbulent kinetic energy and its rate of dissipation involve (for both phases) various sources terms, such as $\Pi_{k,ep}$, $\Pi_{k,e\rho}$ and $\Pi_{k,s\rho}$, that are missing in the corresponding balance equations of the OS model. Furthermore, in the Reynolds-averaged granular internal energy balance equation (Eq. (2.17), but see also Eq. (2.42)), the OS model expresses $\boldsymbol{S}_s(\langle\alpha_s\rangle, \langle\theta_s\rangle_S) : \partial_{\boldsymbol{x}} \langle \boldsymbol{u}_s \rangle_S$ in terms of the total solid stress tensor $-\boldsymbol{S}_{s,l} + \boldsymbol{S}_{s,t}$ – instead of the laminar part only, which is used in the Fox model. The omission of all the additional terms and the use of an incorrect solid stress tensor in Eq. (2.17) may impact the simulation results. These issues are explored in the following sections.

Another distinction between the Fox and OS models lies in the closures adopted for the drift velocity and the turbulent interaction terms. For $\boldsymbol{u}_{dr}$, the first model employs the closure reported by Fox (2014), given by Eq. (2.39), while the OS model generally employs those by Burns et al. (2004) and Simonin and Viollet (1990), given by Eqs. (2.53) and (2.54), respectively. For the turbulent interaction terms, the Fox model uses Eqs. (2.45)A, (2.47), (2.49)A and (2.51), whilst the OS model uses those by Simonin and Viollet (1990), given by Eqs. (2.56), (2.58) and (2.61). Nevertheless, the choice of any of these closures is acceptable, regardless of the adopted model; for instance, nothing prevents us from using in the Fox model the drift velocity closure from Burns et al. (2004) or the closures for the turbulent interaction terms by Simonin and Viollet (1990). The same is true for the drag force closures, such as the HG model and SB model: all of them are acceptable, thus one should select those that yield the most accurate results. In the next sections, we also assess the impact of these closures to guide their selection in multiphase flow modeling.

3.2. Experimental system and operating conditions

To validate the results of the models, we use the experimental data of Guida et al. (2010), because they cover a broad range of solid volume fractions (2.5%–23.6%) and provide reasonably detailed velocity and volume fraction spatial profiles. The experiments were conducted in a flat-bottom cylindrical vessel with an open top and four baffles. The vessel diameter T was 288 mm, the width of the baffles W was $0.1T$, and the height of the suspension in the vessel H was equal to the vessel diameter T. The impeller, a 6-blade 45° pitched blade turbine, operated in a down-pumping mode, its off-bottom clearance C, diameter D and height L being equal to $0.25T$, $0.5T$ and $0.1T$, respectively. The fluid density and viscosity were 1150 kg/m^3 and 0.001 Pa · s; the spherical particles had size between 2.85 to 3.30 mm, with a density of 2485 kg/m^3. The experiments were performed at four mean solid volume fractions, $\alpha_{s,0} = 2.5\%, 5.2\%, 10.4\%, 23.6\%$, with four corresponding impeller rotation speeds, $N = 6.00, 6.75, 8.00, 9.83$ rounds per second (rps), respectively. We consider only the experiments with the smallest and largest solid volume fractions (i.e., $\alpha_{s,0} = 2.5\%, 23.6\%$).

3.3. Computational setup

For flow problems involving agitated vessels, the sliding mesh (SM) and the multiple reference frame (MRF) numerical methods are commonly used. In baffled vessels, the relative position between the impeller and the baffles changes over time, so the flow is always transient. The SM method offers accurate solutions for these problems but is extremely demanding computationally and so impractical. The MRF method is a convenient alternative that yields approximate, but often sufficiently good, solutions at a far lower computational cost. In this study, we verify the applicability of this method for our problem of interest by comparing its results to those of the SM method. The simulations are performed in the computational fluid dynamics (CFD) software Fluent. Then, for further simulations, we adopt the MRF method. The reference moving zone has a radius of 94 mm and its lower and upper boundaries are located at 37 mm and 107 mm from the bottom of the vessel. Furthermore, we take the particle diameter to be 3 mm and the restitution coefficient to be 0.95 (Wadnerkar et al., 2016). Owing to the presence of baffles, at the top of the vessel the gas–liquid interface is almost flat; hence, we take this boundary to be flat and therein require the shear stress for both the liquid and solid phases to be zero. This allows disregarding the flow in the gas phase, simplifying the simulations considerably. The surfaces of the rod and impeller are treated as rotating moving walls, while the remaining walls are treated as stationary; on all the walls, no-slip boundary conditions are applied to both phases. Finally, we assume that initially the solid is uniformly distributed in the flow domain.

3.4. Work plan

Initially, adopting the Fox model outlined in Section 2.1.2 with the closures presented in Section 2.2.2 (with the drag coefficient calculated via the HG model) and the MRF method, we perform a mesh independence analysis. Here, the values of the parameters C_g and C_p (featuring in Eqs. (2.36) and (2.39)) are set to zero. Once the appropriate mesh is identified, we employ it for all the other simulations. After, we use the SM method to verify the applicability of the MRF method, running all the subsequent simulations with the latter. Then, we vary C_g and C_p to evaluate their effect and obtain their values. We go on to study the impact of the closures discussed in Section 2.2.2 and select those that yield the best results, concluding the work by analyzing the differences between the Fox and OS models.

4. Results and discussion

4.1. Mesh independence

To ensure computational accuracy, we consider three meshes with 781,920, 1,154,083 and 1,627,825 cells to simulate the experiment of Guida et al. (2010) involving the suspension with a mean solid volume fraction of 23.6%. Fig. 1a reports the axial profiles of the azimuthally and radially-averaged solid volume fraction (or, equivalently, the solid volume fraction averaged over horizontal planes at various heights), normalized by the mean solid volume fraction $\alpha_{s,0}$. In addition, in the Supplementary Information, we report the radial profiles of the normalized azimuthally-averaged solid volume fraction at several heights z and of the normalized (by the speed at the tip of the blade u_{tip}) azimuthally-averaged velocity components of both phases at the height $z = 0.2H$ (the lower edge of the impeller blade). As we see, changing from the mesh with 1,154,083 cells to that with 1,627,825 cells leads to minimal changes in simulation results. Consequently, for all the subsequent simulations, we employ the mesh with 1,154,083 cells.

4.2. SM method versus MRF method

The simulation described in Section 4.1 adopted the MRF method; we now repeat it using the SM method. It is found that, after several impeller rotations, the simulation results (i.e., the profiles of the spatially-averaged quantities mentioned before) depend on time very mildly. Even so, in Fig. 1b we report the results averaged over three consecutive seconds; time-averaged radial profiles of the solid volume fraction and of the velocity components are shown in the Supplementary Information. The results from the SM and MRF methods differ negligibly, validating the applicability of the MRF method for future simulations.

4.3. Sensitivity analysis

We now conduct a sensitivity analysis to see how C_g and C_p affect the numerical results and to find suitable values for these parameters. First, we set C_p to zero and change C_g between 0 and 0.9. As Fig. 1c indicates, setting $C_g = 0$ produces simulation results that align more closely with the experimental axial profile of the solid volume fraction. As shown in the Supplementary Information, this is also generally true for the radial solid volume fraction profiles at different heights along the axis of the vessel. While setting $C_g = 0.9$ slightly improves the prediction of the radial profiles of the velocity components, this improvement is localized at the specific plane $z = 0.2H$, not being generally observed. Since the solid volume fraction distribution depends on the velocity distribution, the more accurate predictions of the axial and radial profiles of the solid volume fraction when $C_g = 0$ suggest a more accurate velocity prediction throughout the vessel. So, we set $C_g = 0$. Now, we vary the value of C_p between zero and unity. As shown in Fig. 1c, $C_p = 0$ yields better results for the axial solid volume fraction profile. As seen in the Supplementary Information, in general this is also true for the radial profiles of solid volume fraction and velocity components. Thus, we set $C_p = 0$.

4.4. Comparison of different closures

As discussed, to effectively compare the Fox and OS models, we must employ in both the same closures. In doing this, we should select the closures that yield the most accurate predictions. In this section, we aim to do this, using the Fox model and investigating how different closures for the drift velocity, turbulent interaction terms and drag coefficient affect the numerical results. The closures giving the most accurate results are then used for subsequent analysis. The simulated cases are outlined in Table 1. Case 1, Case 2 and Case 3 differ in the closure for the drift velocity, Case 4 and Case 1 in the closure for the turbulent interaction terms, while Case 5 and Case 1 in the closure for the drag coefficient.

4.4.1. Low mean solid volume fraction

First, we consider the case with $\alpha_{s,0} = 2.5\%$. Fig. 2 compares the axial profiles of the solid volume fraction, averaged over horizontal planes, found numerically with the experimental profile. The corresponding radial profiles at various heights are given in the Supplementary Information. The experimental data indicate that in the vertical direction the particles are distributed non-uniformly, their volume fraction being higher below the impeller and decreasing gradually in the upper vessel region. As Fig. 2a indicates, the three drift velocity closures lead to identical results, which closely align with the experimental values in the upper region of the vessel and overestimate them near the impeller. Based on these results, we do not have a specific closure for the drift velocity to recommend. As shown in Fig. 2b, the overestimation is more pronounced when the turbulent interaction terms are modeled with the closure of Simonin et al. (1990), while, as shown in Fig. 2c, using the SB model instead of the HG model reduces the overestimation. Moreover,

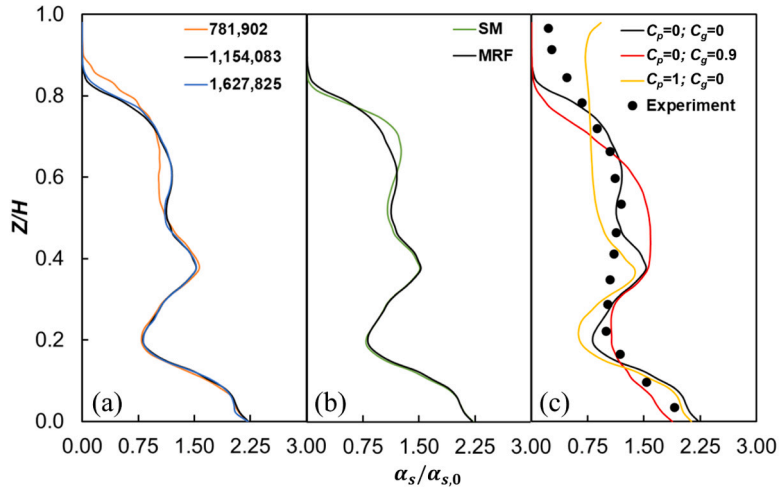

Fig. 1. Comparison of the axial profiles of the normalized azimuthally and radially-averaged solid volume fraction with various (a) computational meshes, (b) computational methods and (c) values of the parameters C_g and C_p for $\alpha_{s,0} = 23.6\%$.

Table 1
Cases for analyzing the effect of closures.

	Drift velocity	Turbulent interaction terms	Drag coefficient
Case 1	Model by Fox (2014)	Model by Fox (2014)	HG model
Case 2	Model by Burns et al. (2004)	Model by Fox (2014)	HG model
Case 3	Model by Simonin and Viollet (1990)	Model by Fox (2014)	HG model
Case 4	Model by Fox (2014)	Model by Simonin et al. (1990)	HG model
Case 5	Model by Fox (2014)	Model by Fox (2014)	SB model

* For the drift velocity, the closure by Fox (2014) refers to Eq. (2.39), that by Burns et al. (2004) to Eq. (2.53), while that by Simonin and Viollet (1990) to Eq. (2.54). The closure for the turbulence interaction terms by Fox (2014) refers to Eqs. (2.45)A, (2.47), (2.49)A and (2.51), while the closure by Simonin et al. (1990) refers to Eqs. (2.56), (2.58) and (2.61). The HG and SB models refer to Eqs. (2.26) and (2.28), respectively.

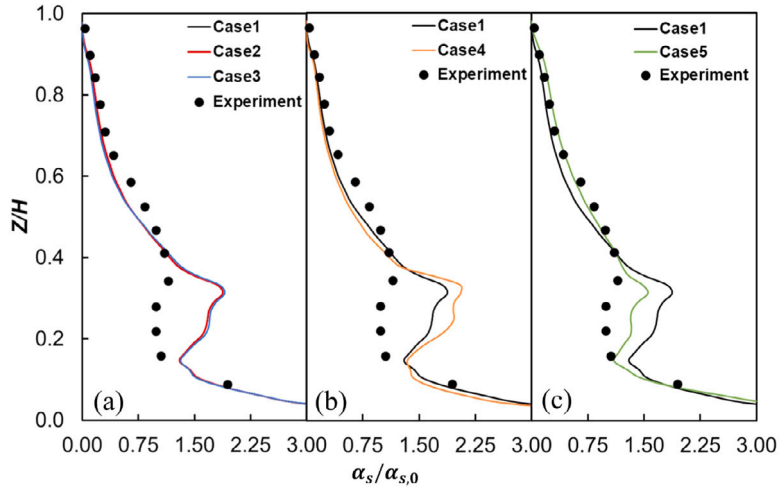

Fig. 2. Comparison between simulation results using different closures and experimental data of the axial profiles of the normalized azimuthally and radially-averaged solid volume fractions for $\alpha_{s,0} = 2.5\%$.

the SB model slightly improves the numerical results across the whole vessel.

Fig. 3 shows the radial profiles of the normalized azimuthally-averaged velocity components at the height $z = 0.2H$ for both the fluid and solid phases, comparing experimental data to simulation results. The former indicate that the axial velocity is predominant, surpassing the moderate tangential velocity and the minimal radial velocity. This pattern is influenced by the axially-dispersing impeller — a pitched blade down-pumping turbine. As the radial coordinate increases in the impeller plane, the magnitude of the axial velocity initially increases (the flow being directed downwards), for the blade velocity is proportional to the radial coordinate, then reduces (where the impeller ends), and finally rises near the tank wall (the flow being directed upwards). This flow pattern, correctly captured by the simulations, is attributed

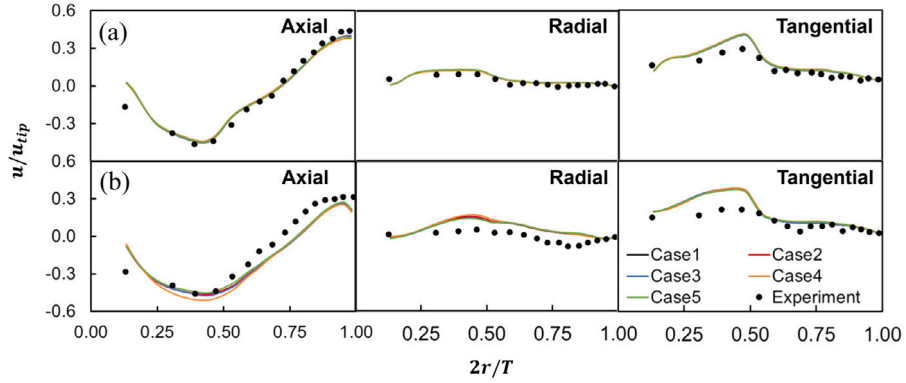

Fig. 3. Comparison between simulation results using different closures and experimental data of the radial profiles of the normalized azimuthally-averaged velocity components of (a) the liquid phase and (b) the solid phase at the horizontal plane $z = 0.2H$ for $\alpha_{s,0} = 2.5\%$.

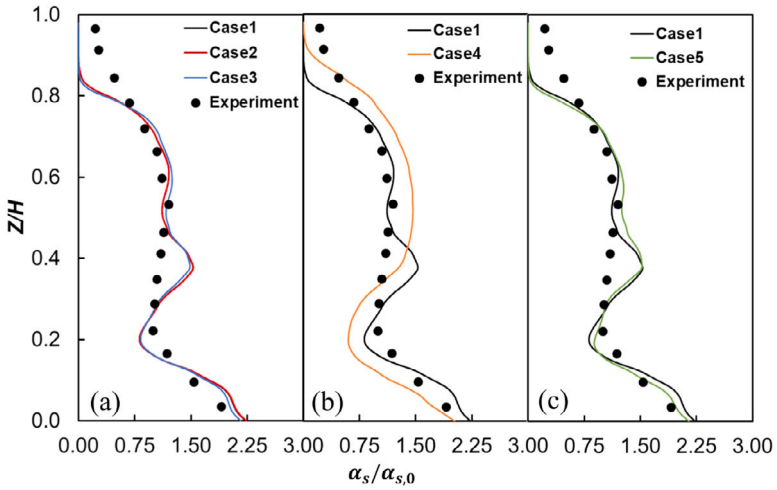

Fig. 4. Comparison between simulation results using different closures and experimental data of the axial profiles of the normalized azimuthally and radially-averaged solid volume fraction for $\alpha_{s,0} = 23.6\%$.

to the formation of a flow loop close to the impeller (Guida et al., 2010). The tangential and radial components of the velocity vector mildly increase with the radial coordinate until peaking at the blade tip; this is followed by a slight decline due to the absence of momentum contributions from the impeller. These velocity profiles are also well captured numerically. As Fig. 3 shows, for all the cases considered in Table 1, and for both phases, the results are nearly identical. For the liquid phase, as seen in Fig. 3a, the predicted axial and radial velocities align well with the experimental data, while a mild overestimation in the tangential velocity is observed near the blade tip. Similarly, as shown in Fig. 3b, for the solid phase only minor differences are found between the predictions and the experimental data of the velocity components.

4.4.2. High mean solid volume fraction

We now focus on the case with a higher solid volume fraction, $\alpha_{s,0} = 23.6\%$. Fig. 4 reports the solid volume fraction axial profiles, comparing numerical results to experimental data. The corresponding radial profiles at several heights are presented in the Supplementary Information. As observed, the distribution of the solid volume fraction is qualitatively similar to that of the lower volume fraction case. As seen in Fig. 4a, again the three drift velocity closures lead to almost the same predictions. Although there is a slight underestimation of the solid volume fraction near the vessel top and just below the impeller, as well as a mild overestimation just above the impeller, the overall agreement between the simulation results and the experimental data is quite good. As shown in Fig. 4b, also now using the closures by Simonin et al. (1990) for the turbulent interaction terms increases the discrepancy between the predictions and the experimental data. However, as seen in Fig. 4c, at the higher concentration of $\alpha_{s,0} = 23.6\%$ using the SB closure for the drag coefficient does not affect significantly the prediction of the solid volume fraction profile.

Fig. 5 reports simulation results and experimental data for the velocity component radial profiles for both phases at the horizontal plane $z = 0.2H$. Qualitatively, the experimental data are similar to those for the case where $\alpha_{s,0} = 2.5\%$. For the liquid phase, the velocity profiles generated by the various closures are relatively close to each other; compared to the experimental data, the magnitude of the axial velocity is underestimated, whilst the magnitudes of the radial and tangential velocities are overpredicted for most radial locations. But these differences are minor (also considering that for the experimental data no error bars are available), so the overall agreement between simulation results and experimental data is acceptable. For the solid phase, the drift velocity closures lead to almost the same results. Furthermore, using different closures for the turbulent interaction terms affects the tangential velocity minimally, while minor deviations are observed for the radial and axial velocities. Specifically, the closure by Simonin et al. (1990) reduces the radial velocity, improving the agreement with the experimental data; but this closure is not superior, because it results in a solid volume fraction distribution that deviates

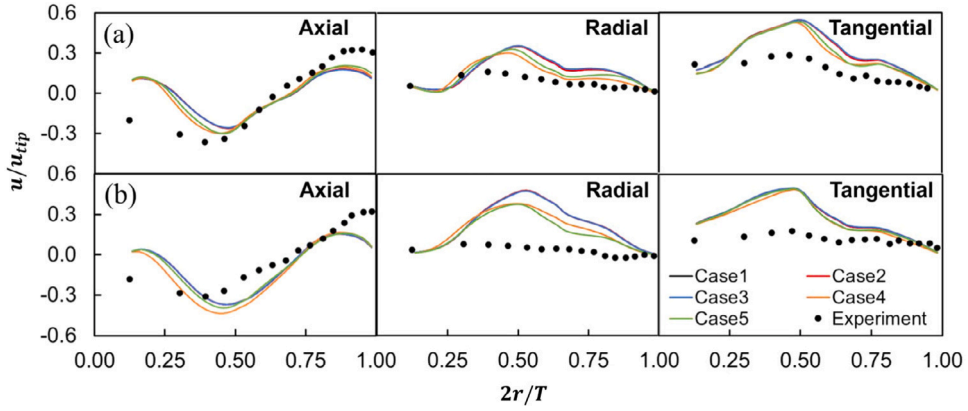

Fig. 5. Comparison between simulation results using different closures and experimental data of the radial profiles of the normalized azimuthally-averaged velocity components of (a) the liquid phase and (b) the solid phase at the horizontal plane $z = 0.2H$ for $\alpha_{s,0} = 23.6\%$.

more from the experimental data (see Fig. 4b). Finally, switching from the HG model to the SB model has only a marginal effect on the axial and tangential velocities, but it reduces the radial velocity, enhancing the agreement with the experimental data.

4.4.3. Conclusions of the closure analysis

The closures for the drift velocity yield nearly identical predictions, while those for the turbulent interaction terms used in the Fox model and the SB model for the drag coefficient tend to generate results that align more closely with the experimental data. Accordingly, in what follows we employ the closures applied in Case 5. Moreover, the results of this analysis suggest that the Fox model can describe liquid–particle turbulent flows in agitated vessels with sufficient accuracy.

4.5. Fox model versus OS model — Part 1

In this section, we explore the impact of the differences between the Fox model and the OS model, focusing on the additional terms generated by the Reynolds averaging process, which the Fox model considers and the OS model neglects, and on the stress tensor adopted in the term $\boldsymbol{S}_s(\langle\alpha_s\rangle, \langle\theta_s\rangle_S) : \partial_{\boldsymbol{x}}\langle\boldsymbol{u}_s\rangle_S$ featuring in the Reynolds-averaged granular internal energy balance equation (Eq. (2.17), but see also Eq. (2.42)). As discussed, the stress tensor that should be used in this term is the laminar part of the total solid stress tensor, but various researchers have instead used the total solid stress tensor, including the turbulent part. To assess the influence of these factors, we consider only one term at a time; the cases considered are reported in Table 2. As in the Fox model we set $C_p = 0$ (see Section 4.3), in this analysis we do not consider the terms generated by the Reynolds-averaging process that involve this parameter, such as the term $\langle\alpha_s'\partial_{\boldsymbol{x}}p_e'\rangle$ (related to the buoyancy force; see Eqs. (2.35) and (2.36)) or the part of $\Pi_{k,s\rho}$ related to C_p (see Eq. (2.49)). Here, all the simulations are performed using the Fox model.

4.5.1. Low mean solid volume fraction

First, we analyze the case with $\alpha_{s,0} = 2.5\%$. Fig. 6 reports the experimental and numerical axial profiles of the normalized solid volume fraction averaged over horizontal planes. The corresponding radial profiles at several heights along the axis of the vessel are shown in the Supplementary Information. The radial profiles of the normalized velocity components are reported, for both phases, in Fig. 7. Cases 6, 8 and 9 yield results that are nearly identical to those of Case 5 (the reference case); i.e., neglecting the turbulent flux of granular internal energy or the terms $\Pi_{k,ep}$, $\Pi_{k,e\rho}$ and $\Pi_{k,s\rho}$ does not alter the profiles of the solid volume fraction and velocity components. Also Case 10 gives results that are very close to those of the reference case. But when the granular internal energy source is excluded (Case 7), while minor

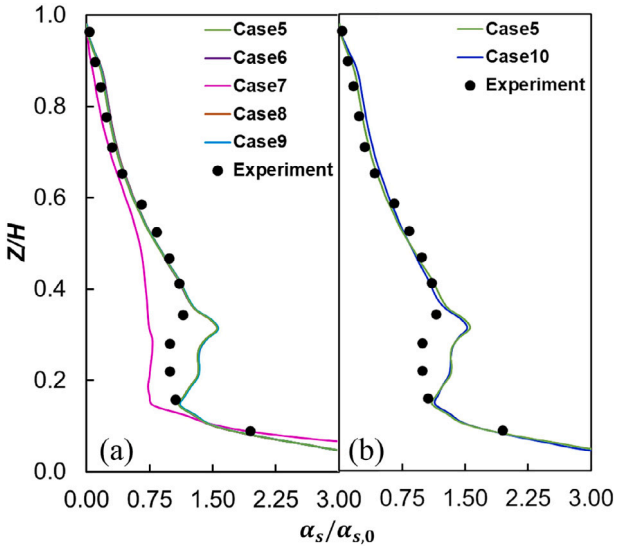

Fig. 6. Effects of (a) the additional terms in the Fox model and (b) the solid stress tensor used in the term $\boldsymbol{S}_s(\langle\alpha_s\rangle, \langle\theta_s\rangle_S) : \partial_{\boldsymbol{x}}\langle\boldsymbol{u}_s\rangle_S$ featuring in the Reynolds-averaged granular internal energy balance equation on the simulation results of the axial profiles of the normalized azimuthally and radially-averaged solid volume fractions for $\alpha_{s,0} = 2.5\%$.

changes are observed in the velocity profiles at the plane $z = 0.2H$, notable changes occur in the predicted solid volume fraction distribution; in particular, particles accumulate near the bottom of the vessel, whilst in the remaining part, especially in the area just above the impeller, the solid volume fraction reduces, leading to an underestimation of the measured values. However, the deviation between predictions and experimental data remains acceptable.

4.5.2. High mean solid volume fraction

In this section, we focus on the case with a higher particle concentration, $\alpha_{s,0} = 23.6\%$. Figs. 8 and 9 report the usual experimental and numerical profiles for the cases considered in Table 2. Radial profiles of the solid volume fraction at several heights along the vessel axis are shown in the Supplementary Information. Similar to the case with $\alpha_{s,0} = 2.5\%$, Cases 6, 8, 9 and 10 yield nearly identical results to those of the reference case. In contrast, neglecting the source term in Eq. (2.17) increases the solid volume fraction near the top and bottom of the vessel, reducing it in the middle; while this leads to a better agreement with the experimental data away from the bottom, an overestimation near the bottom appears. Neglecting the source term alters negligibly

Table 2
Cases used in the analysis of the differences between the Fox and OS models.

	Turbulent flux	Source	$\Pi_{k,ep}$	$\Pi_{k,ep}$ and $\Pi_{k,sp}$	Solid stress tensor
Case 5	✓	✓	✓	✓	L
Case 6	×	✓	✓	✓	L
Case 7	✓	×	✓	✓	L
Case 8	✓	✓	×	✓	L
Case 9	✓	✓	✓	×	L
Case 10	✓	✓	✓	✓	E

* "Turbulent flux" and "Source" refer to the turbulent flux of granular internal energy (Eq. (2.40)) and to the generation of granular internal energy owing to the dissipation of solid turbulent kinetic energy (Eq. (2.43)), respectively, in the Reynolds-averaged granular internal energy balance equation (Eq. (2.17)). $\Pi_{k,ep}$ is the source term owing to the gradient of the Reynolds-averaged fluid pressure (Eq. (2.45)), while $\Pi_{k,ep}$ and $\Pi_{k,sp}$ are the source terms owing to the covariance of the fluctuations of the Eulerian fluid velocity and fluid pressure gradient (Eqs. (2.45) and (2.49)). ✓indicates that these terms are included, while ×indicates that they are excluded. "Solid stress tensor" refers to the stress tensor used in the term $\boldsymbol{S}_s(\langle\alpha_s\rangle,\langle\theta_s\rangle_s) : \partial_{\boldsymbol{x}}\langle\boldsymbol{u}_s\rangle_s$ featuring in the Reynolds-averaged granular internal energy balance equation (see also Eq. (2.42)), where E denotes the use of the entire solid stress tensor, while L denotes the use of the laminar part only.

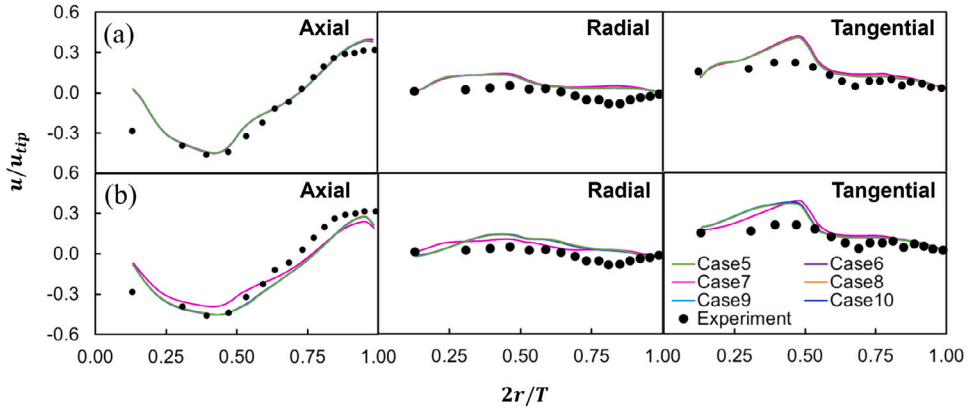

Fig. 7. Effects of the differences between the Fox model and the OS model on the simulation results of the radial profiles of the normalized azimuthally-averaged velocity components of (a) the liquid phase and (b) the solid phase at the horizontal plane $z = 0.2H$ for $\alpha_{s,0} = 2.5\%$.

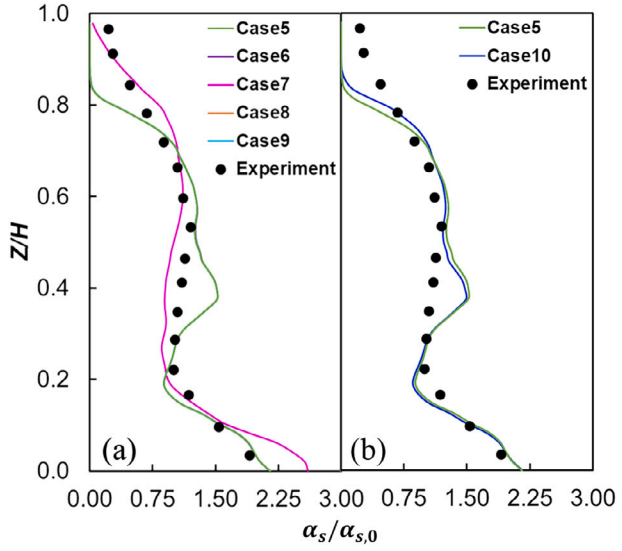

Fig. 8. Effects of (a) the additional terms in the Fox model and (b) the solid stress tensor used in the term $\boldsymbol{S}_s(\langle\alpha_s\rangle,\langle\theta_s\rangle_s) : \partial_{\boldsymbol{x}}\langle\boldsymbol{u}_s\rangle_s$ featuring in the Reynolds-averaged granular internal energy balance equation on the simulation results of the axial profiles of the normalized azimuthally and radially-averaged solid volume fractions for $\alpha_{s,0} = 23.6\%$.

the velocity components of the liquid phase and the axial and tangential velocity components of the solid phase, but reduces the solid-phase radial velocity component, overestimating less the experimental data.

In light of these results, it is clear that – at least for the cases herein examined – only the granular internal energy source term affects the simulation results appreciably. However, this change is not significant enough to alter the overall simulation accuracy, and the alignment between experimental data and simulation results remains generally acceptable. Nevertheless, this source term is quite important conceptually, and so it should be accounted for.

4.6. Fox model versus OS model — Part 2

Now, we compare the results of the Fox model with those of the OS model. In the Fox model, we employ the closures of Case 5; in the OS model, in line with what we discussed in Sections 2 and 3, the turbulent flux and source term of granular internal energy, as well as the terms $\Pi_{k,ep}$, $\Pi_{k,ep}$ and $\Pi_{k,sp}$, are neglected, while the term $\boldsymbol{S}_s(\langle\alpha_s\rangle,\langle\theta_s\rangle_s) : \partial_{\boldsymbol{x}}\langle\boldsymbol{u}_s\rangle_s$ is replaced with $(\boldsymbol{S}_{e,l} + \boldsymbol{S}_{e,t}) : \partial_{\boldsymbol{x}}\boldsymbol{u}_s$. According to the analysis in Section 4.5, based on the Fox model, only the granular internal energy source term impacts the model predictions, so we expect that the predictions of the OS model should be close to those of Case 7, where the granular internal energy source term is omitted in the Fox model. As we can see in Figs. 10 through 12, this expectation is confirmed: the OS model and the Fox model with the setup of Case 7 yield nearly identical predictions for the axial profiles of the solid volume fraction and the radial profiles of the velocity components. This is also true for the solid volume fraction radial profiles reported

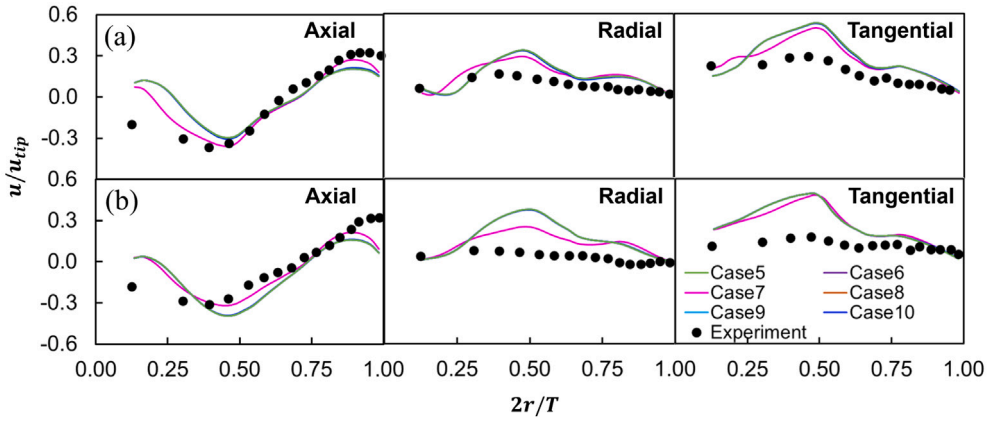

Fig. 9. Effects of the differences between the Fox model and the OS model on the simulation results of the radial profiles of the normalized azimuthally-averaged velocity components of (a) the liquid phase and (b) the solid phase at the horizontal plane $z = 0.2H$ for $\alpha_{s,0} = 23.6\%$.

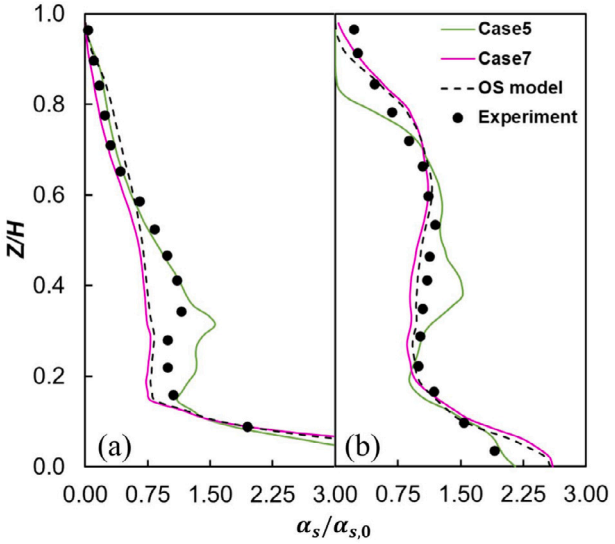

Fig. 10. Comparisons of the numerical axial profiles of the normalized azimuthally and radially-averaged solid volume fraction obtained from the Fox and OS models for (a) $\alpha_{s,0} = 2.5\%$ and (b) $\alpha_{s,0} = 23.6\%$.

in the Supplementary Information. This implies that the discussion of Case 7 in Section 4.5 applies to the OS model as well. We conclude that – at least for the cases considered in this work – the difference in predictions between the Fox and OS models is solely due to the granular internal energy source term featuring in Eq. (2.17). But this deviation is not enough to affect the numerical results considerably. However, although the OS model can produce desired results, its derivation, as discussed in Section 2.1.3, remains theoretically unjustified. Moreover, we should keep in mind that our conclusions are valid only for the cases herein analyzed; nothing guarantees that for other systems the terms neglected or incorrectly expressed in the OS model affect the results negligibly. Therefore, in general we do recommend considering these terms. Their implementation in a commercial solver is reasonably simple, but accounting for them does increase the computational time; for instance, the addition of the granular internal energy source term alone increases it by over 50%. To optimize the computational resources whilst ensuring accuracy, we suggest assessing the importance of each term under the conditions of interest, employing the approach demonstrated in this work.

5. Conclusions

In this work, we critically analyzed turbulent multifluid models derived from the Eulerian–Eulerian equations of change, focusing on their application for simulating liquid–particle turbulent flows in agitated vessels. In particular, we investigated the Fox and OS models. Obtained by Reynolds-averaging the Eulerian–Eulerian equations, the Fox model is theoretically robust. In contrast, the OS model lacks theoretical justification, as it is not derived rigorously via averaging but features terms that are just added to account for the main effects of turbulence. Despite this, this model is widely adopted and often produces favorable results. Our analysis reveals that, when the Eulerian variables in the OS model are replaced with their corresponding Reynolds or phase averages, the differences between the two models mainly arise from additional terms (generated by the averaging process) specific to the Fox model and from the solid stress tensor used to express the source term $\langle \boldsymbol{S}_s : \partial_{\boldsymbol{x}} \boldsymbol{u}_s \rangle$ in the Reynolds-averaged granular internal energy balance equation.

To investigate the effects of these differences and compare the predictions of the Fox and OS models, we first adopted the Fox model to assess the effect of various closures for the undetermined terms featuring in the model. Our findings indicate that the closures that we considered for the drift velocity yield nearly identical results for the volume fraction and the velocity components profiles. On the other hand, the closures for the turbulent interaction terms and the drag coefficient influence the results. In particular, the closures proposed by Fox (2014) for the turbulent interaction terms and by Syamlal et al. (1993) for the drag coefficient yield results that better align with experimental data.

Adopting the closures that yield better predictions, we then conducted simulations to evaluate the impact of the differences between the Fox model and the OS model. Our analysis showed that some of the additional terms present in the Fox model (arising from the Reynolds averaging process) and the solid stress tensor used in the source term $\langle \boldsymbol{S}_s : \partial_{\boldsymbol{x}} \boldsymbol{u}_s \rangle$ in the Reynolds-averaged granular internal energy balance equation affect the results minimally, while the granular internal energy source term related to the dissipation of solid turbulent kinetic energy impacts the results appreciably. Due to the small influence of the other factors, the differences in the predictions between the Fox and OS models are attributed to this source term. But these differences are not significant enough to reduce the overall accuracy of the simulations. This observation might explain why, even if theoretically unjustified, the OS model often gives satisfactory results.

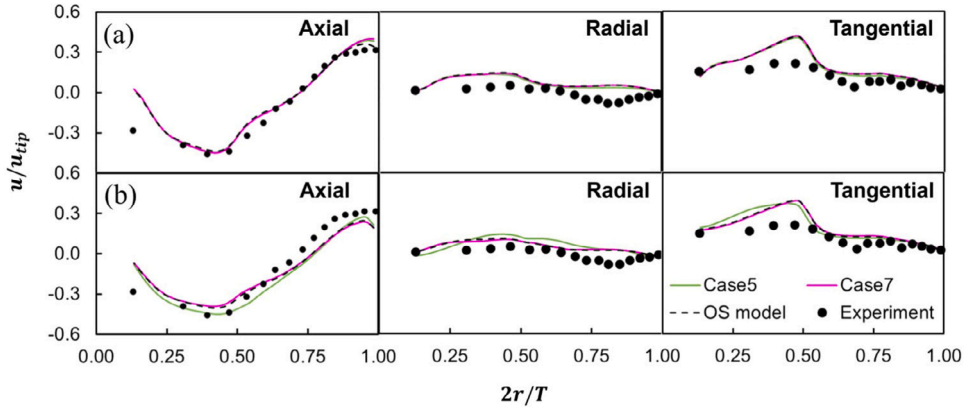

Fig. 11. Comparison of the numerical radial profiles of the normalized azimuthally-averaged velocity components of (a) the liquid phase and (b) the solid phase at the horizontal plane $z = 0.2H$ obtained from the Fox and OS models for $\alpha_{s,0} = 2.5\%$.

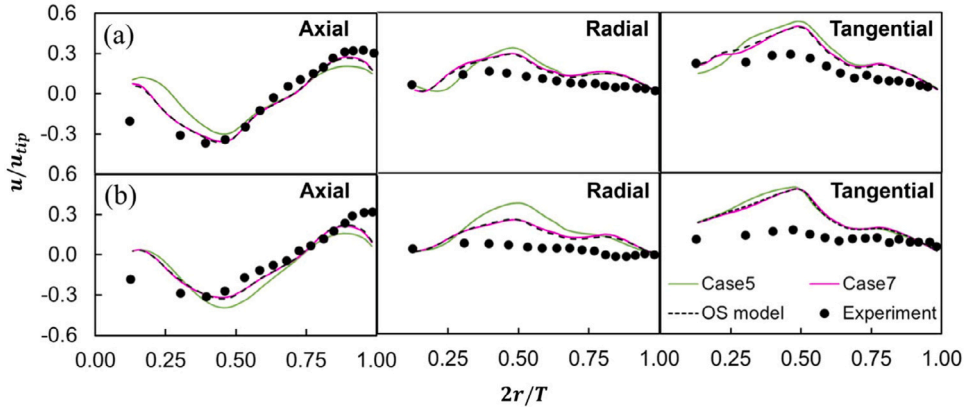

Fig. 12. Comparison of the numerical radial profiles of the normalized azimuthally-averaged velocity components of (a) the liquid phase and (b) the solid phase at the horizontal plane $z = 0.2H$ obtained from the Fox and OS models for $\alpha_{s,0} = 23.6\%$.

CRediT authorship contribution statement

Ziming Wang: Writing – original draft, Visualization, Validation, Methodology, Investigation, Formal analysis, Data curation, Conceptualization. **Luca Mazzei:** Writing – review & editing, Supervision, Project administration, Methodology, Funding acquisition, Conceptualization.

Declaration of competing interest

The authors declare the following financial interests/personal relationships which may be considered as potential competing interests: Ziming Wang reports financial support was provided by GSK. If there are other authors, they declare that they have no known competing financial interests or personal relationships that could have appeared to influence the work reported in this paper.

Acknowledgments

Funding from GlaxoSmithKline (UK) is gratefully acknowledged.

Appendix A. Supplementary data

In the first section of the supplementary material document, to facilitate the comparison between the Fox and OS models, we report their balance equations in closed form, directly including the closures given in Section 2.2 of the main article. In the second section, we report additional simulation results. First, we report those related to the grid independence analysis. Then, we compare the predictions of the SM and MRF methods in terms of radial profiles of solid volume fraction and velocity components. This is followed by a sensitivity analysis on the parameters C_g and C_p introduced in Section 2.2.2 of the main article. In the final part of the document, we present simulation and experimental results related to solid volume fraction radial profiles for the cases reported in Tables 1 and 2 of the main article.

Supplementary material related to this article can be found online at https://doi.org/10.1016/j.cherd.2025.05.023.

References

Ahmadi, G., Ma, D., 1990. A thermodynamical formulation for dispersed multiphase turbulent flows-1: Basic theory. Int. J. Multiph. Flow 16 (2), 323–340.

Altway, A., Setyawan, H., Winardi, S., et al., 2001. Effect of particle size on simulation of three-dimensional solid dispersion in stirred tank. Chem. Eng. Res. Des. 79 (8), 1011–1016.

Astarita, G., 1993. Forces acting on particles in a fluidized bed. Chem. Eng. Sci. 48 (19), 3438–3440.

Battista, F., Gualtieri, P., Mollicone, J., Casciola, C., 2018. Application of the exact regularized point particle method (ERPP) to particle laden turbulent shear flows in the two-way coupling regime. Int. J. Multiph. Flow 101, 113–124.

Brilliantov, N.V., Pöschel, T., 2004. Kinetic Theory of Granular Gases. Oxford University Press.

Burns, A.D., Frank, T., Hamill, I., Shi, J.M., et al., 2004. The favre averaged drag model for turbulent dispersion in Eulerian multi-phase flows. In: 5th International Conference on Multiphase Flow, ICMF, vol. 4, ICMF, pp. 1–17.

Buyevich, Y.A., 1999. Particulate stresses in dense disperse flow. Ind. Eng. Chem. Res. 38 (3), 731–743.

Calvo, S., Delafosse, A., Collignon, M.L., Crine, M., Toye, D., 2013. Experimental characterisation and modelling of homogeneous solid suspension in an industrial stirred tank. Adv. Mech. Eng. 5, 329264.

Chapman, S., Cowling, T., 1991. The mathematical theory of non-uniform gases: An account of the kinetic theory of viscosity, thermal conduction and diffusion in gases. In: Cambridge Mathematical Library, Cambridge University Press.
Chen, L., Duan, Y., Pu, W., Zhao, C., 2009. CFD simulation of coal-water slurry flowing in horizontal pipelines. Korean J. Chem. Eng. 26 (4), 1144–1154.
Dasgupta, S., Jackson, R., Sundaresan, S., 1994. Turbulent gas-particle flow in vertical risers. AIChE J. 40 (2), 215–228.
Dasgupta, S., Jackson, R., Sundaresan, S., 1998. Gas-particle flow in vertical pipes with high mass loading of particles. Powder Technol. 96 (1), 6–23.
Deen, N.G., Peters, E., Padding, J.T., Kuipers, J., 2014. Review of direct numerical simulation of fluid-particle mass, momentum and heat transfer in dense gas-solid flows. Chem. Eng. Sci. 116, 710–724.
Delafosse, A., Loubière, C., Calvo, S., Toye, D., Olmos, E., 2018. Solid-liquid suspension of microcarriers in stirred tank bioreactor-experimental and numerical analysis. Chem. Eng. Sci. 180, 52–63.
Di Felice, R., 1994. The voidage function for fluid-particle interaction systems. Int. J. Multiph. Flow 20 (1), 153–159.
Drew, D.A., 1983. Mathematical modeling of two-phase flow. Annu. Rev. Fluid Mech. 15 (1), 261–291.
Enwald, H., Peirano, E., Almstedt, A.E., 1996. Eulerian two-phase flow theory applied to fluidization. Int. J. Multiph. Flow 22, 21–66.
Ergun, S., 1952. Fluid flow through packed columns. Chem. Eng. Prog. 48, 89–94.
Feng, Z.G., Alatawi, E.S., Roig, A., Sarikaya, C., 2016. A resolved Eulerian-Lagrangian simulation of fluidization of 1204 heated spheres in a bed with heat transfer. J. Fluids Eng. 138 (4), 041305.
Foscolo, P.U., Gibilaro, L., Waldram, S., 1983. A unified model for particulate expansion of fluidised beds and flow in fixed porous media. Chem. Eng. Sci. 38 (8), 1251–1260.
Fox, R.O., 2003. Computational Models for Turbulent Reacting Flows. Cambridge University Press.
Fox, R.O., 2014. On multiphase turbulence models for collisional fluid-particle flows. J. Fluid Mech. 742, 368—-424.
Gibb, J., 1991. Pressure and viscous forces in an equilibrium fluidized suspension. Chem. Eng. Sci. 46 (1), 377–379.
Gibilaro, L.G., 2001. Fluidization Dynamics. Elsevier.
Gidaspow, D., 1994. Multiphase Flow and Fluidization: Continuum and Kinetic Theory Descriptions. Academic Press.
Gidaspow, D., Huang, J., 2009. Kinetic theory-based model for blood flow and its viscosity. Ann. Biomed. Eng. 37 (8), 1534–1545.
Gualtieri, P., Battista, F., Casciola, C.M., 2017. Turbulence modulation in heavy-loaded suspensions of tiny particles. Phys. Rev. Fluids 2 (3), 034304.
Guida, A., Nienow, A.W., Barigou, M., 2010. PEPT measurements of solid-liquid flow field and spatial phase distribution in concentrated monodisperse stirred suspensions. Chem. Eng. Sci. 65 (6), 1905–1914.
Huilin, L., Gidaspow, D., Bouillard, J., Wentie, L., 2003. Hydrodynamic simulation of gas-solid flow in a riser using kinetic theory of granular flow. Chem. Eng. J. 95 (1–3), 1–13.
Jackson, R., 1997. Locally averaged equations of motion for a mixture of identical spherical particles and a Newtonian fluid. Chem. Eng. Sci. 52 (15), 2457–2469.
Jackson, R., 2000. The Dynamics of Fluidized Particles. Cambridge University Press.
Jamshidi, R., Angeli, P., Mazzei, L., 2019. On the closure problem of the effective stress in the Eulerian-Eulerian and mixture modeling approaches for the simulation of liquid-particle suspensions. Phys. Fluids 31 (1), 013302.
Jamshidi, R., Gillissen, J.J.J., Angeli, P., Mazzei, L., 2021. Roles of solid effective stress and fluid-particle interaction force in modeling shear-induced particle migration in non-Brownian suspensions. Phys. Rev. Fluids 6 (1), 014301.
Jiang, Y., Zhang, P., 2012. Numerical investigation of slush nitrogen flow in a horizontal pipe. Chem. Eng. Sci. 73, 169–180.
Kasat, G., Khopkar, A., Ranade, V.V., Pandit, A.B., 2008. CFD simulation of liquid-phase mixing in solid-liquid stirred reactor. Chem. Eng. Sci. 63 (15), 3877–3885.
Kaushal, D., Thinglas, T., Tomita, Y., Kuchii, S., Tsukamoto, H., 2012. CFD modeling for pipeline flow of fine particles at high concentration. Int. J. Multiph. Flow 43, 85–100.
Kazemzadeh, A., Ein-Mozaffari, F., Lohi, A., 2020. Hydrodynamics of solid and liquid phases in a mixing tank containing high solid loading slurry of large particles via tomography and computational fluid dynamics. Powder Technol. 360, 635–648.
Lettieri, P., Mazzei, L., 2009. Challenges and issues on the CFD modeling of fluidized beds: A review. J. Comput. Multiph. Flows 1 (2), 83–131.
Liu, L., Barigou, M., 2014. Experimentally validated computational fluid dynamics simulations of multicomponent hydrodynamics and phase distribution in agitated high solid fraction binary suspensions. Ind. Eng. Chem. Res. 53 (2), 895–908.
Ljungqvist, M., Rasmuson, A., 2001. Numerical simulation of the two-phase flow in an axially stirred vessel. Chem. Eng. Res. Des. 79 (5), 533–546.
Maluta, F., Paglianti, A., Montante, G., 2019. RANS-based predictions of dense solid-liquid suspensions in turbulent stirred tanks. Chem. Eng. Res. Des. 147, 470–482.
Marchisio, D., Fox, R., 2013. Computational models for polydisperse particulate and multiphase systems. In: Cambridge Series in Chemical Engineering, Cambridge University Press.
Mazzei, L., 2008. Eulerian modelling and computational fluid dynamics simulation of mono and polydisperse fluidized suspension (Ph.D. thesis). p. 211, URL https://www.proquest.com/dissertations-theses/eulerian-modelling-computational-fluid-dynamics/docview/1433892803/se-2.
Mazzei, L., 2019. Recent Advances in Modelling Gas-Particle Flows. Springer.
Mazzei, L., Casillo, A., Lettieri, P., Salatino, P., 2010. CFD simulations of segregating fluidized bidisperse mixtures of particles differing in size. Chem. Eng. J. 156 (2), 432–445.
Mazzei, L., Lettieri, P., 2007. A drag force closure for uniformly dispersed fluidized suspensions. Chem. Eng. Sci. 62 (22), 6129–6142.
Ochieng, A., Onyango, M.S., 2008. Drag models, solids concentration and velocity distribution in a stirred tank. Powder Technol. 181 (1), 1–8.
Oke, O., Lettieri, P., Mazzei, L., 2015. An investigation on the mechanics of homogeneous expansion in gas-fluidized beds. Chem. Eng. Sci. 127, 95–105.
Oke, O., Lettieri, P., Salatino, P., Solimene, R., Mazzei, L., 2014. Numerical simulations of lateral solid mixing in gas-fluidized beds. Chem. Eng. Sci. 120, 117–129.
Oshinowo, L.M., Bakker, A., 2002. CFD modeling of solids suspensions in stirred tanks. In: Symposium on Computational Modelling of Metals, Minerals and Materials, TMS Annual Meeting. Seattle, WA, pp. 234–242.
Pan, T.W., Joseph, D., Bai, R., Glowinski, R., Sarin, V., 2002. Fluidization of 1204 spheres: simulation and experiment. J. Fluid Mech. 451, 169–191.
Peirano, E., Leckner, B., 1998. Fundamentals of turbulent gas-solid flows applied to circulating fluidized bed combustion. Prog. Energy Combust. Sci. 24 (4), 259–296.
Pope, S.B., 2000. Turbulent Flows. Cambridge University Press.
Riella, M., Kahraman, R., Tabor, G.R., 2018. Reynolds-averaged two-fluid model prediction of moderately dilute fluid-particle flow over a backward-facing step. Int. J. Multiph. Flow 106, 95–108.
Rumsey, C.L., 2010. Compressibility considerations for kw turbulence models in hypersonic boundary-layer applications. J. Spacecr. Rockets 47 (1), 11–20.
Sardina, G., Schlatter, P., Brandt, L., Picano, F., Casciola, C.M., 2012. Wall accumulation and spatial localization in particle-laden wall flows. J. Fluid Mech. 699, 50–78.
Shan, X., Yu, G., Yang, C., Mao, Z.-S., Zhang, W., 2008. Numerical simulation of liquid-solid flow in an unbaffled stirred tank with a pitched-blade turbine downflow. Ind. Eng. Chem. Res. 47 (9), 2926–2940.
Shi, P., Rzehak, R., 2020. Solid-liquid flow in stirred tanks: Euler-Euler/RANS modeling. Chem. Eng. Sci. 227, 115875.
Simonin, O., Viollet, P.L., 1990. Modelling of turbulent two-phase jets loaded with discrete particles. In: Phenomena in Multiphase Flows, vol. 1990, Hemisphere Publishing Corporation, pp. 259–269.
Simonin, C., Viollet, P.L., et al., 1990. Predictions of an oxygen droplet pulverization in a compressible subsonic coflowing hydrogen flow. Numer. Methods Multiph. Flows 91 (2), 65–82.
Syamlal, M., Rogers, W., O'Brien, T.J., 1993. MFIX documentation theory guide. Technical Report, USDOE Morgantown Energy Technology Center (METC), WV (United States).
Tamburini, A., Cipollina, A., Micale, G., Brucato, A., Ciofalo, M., 2014. Influence of drag and turbulence modelling on CFD predictions of solid-liquid suspensions in stirred vessels. Chem. Eng. Res. Des. 92 (6), 1045–1063.
Wadnerkar, D., Tade, M.O., Pareek, V.K., Utikar, R.P., 2016. CFD simulation of solid-liquid stirred tanks for low to dense solid loading systems. Particuology 29, 16–33.
Wadnerkar, D., Utikar, R.P., Tade, M.O., Pareek, V.K., 2012. CFD simulation of solid-liquid stirred tanks. Adv. Powder Technol. 23 (4), 445–453.
Wang, S., Jiang, X., Wang, R., Wang, X., Yang, S., Zhao, J., Liu, Y., 2017. Numerical simulation of flow behavior of particles in a liquid-solid stirred vessel with baffles. Adv. Powder Technol. 28 (6), 1611–1624.
Wang, J., Wang, S., Zhang, T., Liang, Y., 2013. Numerical investigation of ice slurry isothermal flow in various pipes. Int. J. Refrig. 36 (1), 70–80.
Wen, C.Y., Yu, Y.H., 1966. Mechanics of fluidization. In: Chem. Eng. Prog. Symp. Ser., vol. 62, pp. 100–111.
Wilcox, D., 1998. Turbulence modeling for CFD. DCW Ind. Can..
Yilmaz, F., Kutlar, A.I., Gundogdu, M.Y., 2011. Analysis of drag effects on pulsatile blood flow in a right coronary artery by using Eulerian multiphase model. Korea-Aust. Rheol. J. 23 (2), 89–103.
Zhang, D.Z., Prosperetti, A., 1997. Momentum and energy equations for disperse two-phase flows and their closure for dilute suspensions. Int. J. Multiph. Flow 23 (3), 425–453.